AN EXPERIMENTAL INVESTIGATION OF THE WEAK-LINK PROBLEM IN GRANULAR HIGH-T_c SUPERCONDUCTORS

by

Kevin Poobalan Reddy

Submitted in partial fulfillment of the
requirements for the degree of
Master of Science,
in the
School of Pure and Applied Physics,
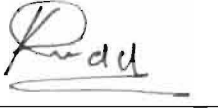University of Natal

Durban
February 2002

To the Glory of the Lord Jesus Christ.

Abstract

Grain boundary weak-link behaviour in superconductors is investigated using a critical state model (CSM), which has been specifically formulated for the applied field range $0 \leq H_a \leq H_{c1g}$, where H_{c1g} is the intra-granular lower critical field. The CSM includes an expression for the inter-granular critical current density, $J_c(H,T)$, that has been derived from a percolation model for a random 3D network of weak-links in which the current flowing through the individual grain boundary junctions is assumed to be spatially random. This expression, namely: $J_c(H,T) = J_{co}[\exp(-H/H_o) + \delta]$, where J_{co}, H_o, and δ are characteristic weak-link parameters, includes a field-dependent component and a field-independent component both of which are microstructurally sensitive. Calculated magnetisation behaviour, obtained from the critical state model, are fitted to experimental isothermal D.C magnetisation data, $M(H_a)$, for $0 \leq H_a \leq H_{c1g}$, 71.5K$\leq T \leq T_c$, obtained from the two control specimens, namely: $Y_1Ba_2Cu_3O_{7-x}$ and $Eu_1Ba_2Cu_3O_{7-x}$, $x \leq 1$, and from a third specimen, which is a mixture of the two control compounds. In the CSM fits, the temperature dependent characteristic parameters J_{co}, H_o, and δ are treated as free fitting parameters. These free fitting parameters are subsequently fitted to specific theoretical models for $J_{co}(T)$, $H_o(T)$, and $\delta(T)$ and a comparison is made between the control specimens and mixed specimen parameters to establish the effect of mixing on the grain boundary weak-link behaviour. J_{co} and δ are found to be significantly larger in the mixed specimen as compared with either of the two control specimens.

Preface

This study represents original work by the author and has not been submitted in any form to another University. Where use was made of the work of others it has been duly acknowledged in the text.

K.P. Reddy

Acknowledgments

The author wishes to thank the following people for the respective roles they played in the compilation of this thesis:

Contents

1 INTRODUCTION TO FUNDAMENTAL THEORY

1.1 Discovery of Superconductivity

In 1911 Kamerling Onnes [1], a Dutch Physicist working at the University of Leiden, observed that the d.c resistance of Mercury suddenly vanished when cooled to the boiling point of liquid helium ($\approx$ 4.2K). He termed this unusual occurrence, "**superconductivity**". Additional experiments carried out by Onnes led to the discovery that relatively weak magnetic fields and electrical currents were capable of destroying the superconducting phase. Roughly two years later Lead was found to exhibit superconductivity at 7.2K. In 1930 Niobium, which is now known to possess the highest critical temperature for all the known metallic elements, was found to be superconducting at 9.2K. See Ref. [2] for details.

1.2 Discovery of High-T_c Superconductivity

For almost 70 years after the discovery of superconductivity by Onnes, all efforts toward the attainment of critical temperatures higher than approximately 23K (Nb_3Ge) [3] had failed. Then, in April 1986, Bednorz and Müller [4], working at IBM in Zurich, published a paper announcing their discovery of the Ba-La-Cu-O superconducting system with a critical temperature of about 30K. Bednorz and Müller were subsequently awarded the Nobel Prize for Physics and contributed to the birth of high-T_c superconductivity.

Inspired by the efforts of Bednorz and Müller, condensed matter physicists and material scientists around the world began working frantically in search of superconducting compounds possessing even higher critical temperatures. Another major breakthrough was realised in 1987 by Wu *et al.* [5] who found that the compound $Y_1Ba_2Cu_3O_{7-x}$ has a superconducting transition temperature T_c of approximately 93K when $x \simeq 0.1$.

Ever since, there has been an unprecedented amount of research toward finding systems with higher T_c's. Critical temperatures above 150K have since been reported by Chu *et al.* [6] for the $HgBa_2Ca_2Cu_3O_{8+x}$ system. Whilst the discovery of the first room-temperature superconductor is an endeavor worth pursuing, the realisation of viable commercial applications of high-T_c systems still remains an important task.

1

1.3 The Meissner-Ochsenfeld Effect

Meissner and Ochsenfeld (1933) discovered that a superconductor (SC), cooled in an applied magnetic field, H_a, less than some critical value, expels all flux from within the interior of the material i.e. the magnetic induction **B** becomes zero as soon as the temperature drops below the transition temperature, T_c. This is illustrated in Fig. 1.

$$T > T_c, H_a > 0 \qquad\qquad T < T_c, H_a > 0$$
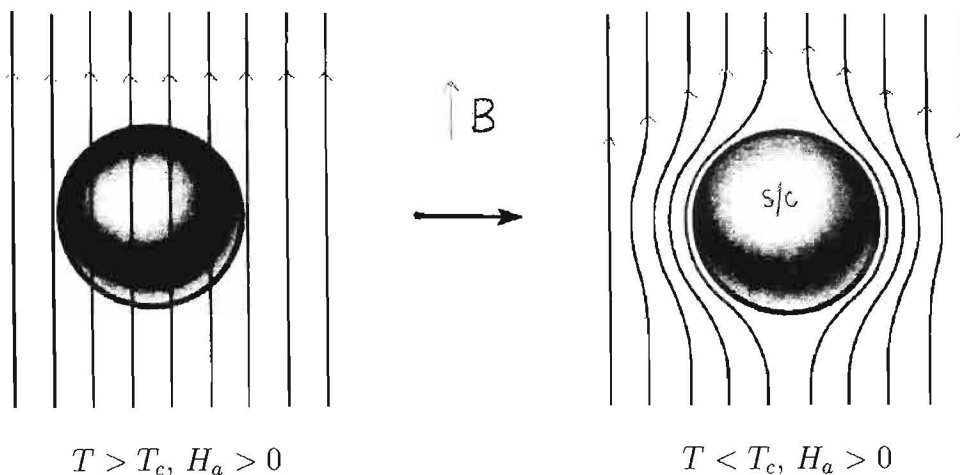
Fig. 1: Illustration of the Meissner effect (from Kittel [7]).

Consider an infinitely long specimen, i.e. with zero demagnetising field, with magnetic field, H_a, applied parallel to its long axis. For $T < T_c$ and $H_a < H_c$, where H_c is some material dependent critical field (see below), the induction **B** inside the specimen is found to be given by $\mathbf{B} = 0 = H_a + 4\pi M$ (emu), where M is the specimen magnetisation. This result is referred to as the "Meissner effect". See Ref. [8] for details on the Meissner-Ochsenfeld effect.

1.4 The Thermodynamic Critical Field, H_c

Below the critical temperature T_c, the free energy density of the superconducting state, f_s, is less than the free energy density of the normal state, f_n. For a monotonically increasing magnetic field, the magnetic energy ($\sim H^2$) slowly changes the balance between f_s and f_n. At some point, the thermodynamic critical field, H_c, is reached, $f_s = f_n$, and the superconducting state is suppressed. Thermodynamic consideration yields an expression [9], namely:

$$f_n - f_s = \frac{H_c^2}{8\pi}. \tag{1}$$

The empirical temperature dependence for H_c is given by [9]:

$$H_c(T) = H_c(0)\left[1 - (T/T_c)^2\right], \tag{2}$$

where $H_c(0) = H_c(T = 0)$.

1.5   The London Equations (1935)

In 1935 London and London [10] published a model for the Meissner effect using the "Two-Fluid Model" proposed by Gorter and Casimir [11]. They assumed that the superconducting fraction, n_s, of the total electron density, n, is not scattered by crystalline impurities or phonons and consequently does not contribute to the electrical resistance.

The equation of motion for superconducting electrons of mass m, and charge e, freely accelerated in an electric field $\mathbf{E}$, is given by

$$m\dot{\mathbf{v}}_\mathbf{s} = e\mathbf{E}, \tag{3}$$

where $\mathbf{v}_\mathbf{s}$ is the superconducting fluid velocity.

The superconducting current,

$$\mathbf{J}_\mathbf{s} = n_s e\mathbf{v}_\mathbf{s}, \tag{4}$$

can then be re-written as

$$\dot{\mathbf{J}}_\mathbf{s} = \left(\frac{n_s e^2}{m}\right)\mathbf{E}. \tag{5}$$

Maxwell's equation relating the electric field $\mathbf{E}$ to the local microscopic field, $\mathbf{h}$ [note: $\mathbf{B}$ is the average of $\mathbf{h}$], is given by

$$\nabla \times \mathbf{E} = -\frac{1}{c}\frac{\partial \mathbf{h}}{\partial t}, \tag{6}$$

where $\mathbf{E} = \rho\mathbf{J}$ (Ohm's law). Substitution of Eq. (5) into Eq. (6), and re-arrangement of terms, yields:

$$\frac{\partial}{\partial t}\left(\nabla \times \mathbf{J} + \frac{n_s e^2}{mc}\mathbf{h}\right) = 0. \tag{7}$$

3

As $\rho \to 0$ (as is the case for a perfect conductor), the left-hand side of Eq. (6) approaches zero resulting in the microscopic field **h**, and hence **B**, being constant and not zero. This contradicts the observations of Meissner and Oschenfeld. Incidentally, we see that the Meissner effect is an inherent feature of the superconducting state and not a consequence of zero resistivity.

To avoid the contradiction F. and H. London therefore integrated Eq. (7) and obtained the particular solution (known as the London equation), namely:

$$\nabla \times \mathbf{J} + \left(\frac{n_s e^2}{mc}\right)\mathbf{h} = 0, \tag{8}$$

which does account for flux expulsion and also provides a definition for the magnetic penetration depth, λ. Substituting Maxwell's equation, namely: $\nabla \times \mathbf{h} = (4\pi/c)\mathbf{J}$, into Eq. (8), and employing the vector identity, namely: $\nabla \times \nabla \times A = \nabla(\nabla \cdot A) - \nabla^2 A$, together with $\nabla \cdot \mathbf{h} = 0$ yeilds:

$$-\nabla^2 \mathbf{h} + \left(\frac{4\pi n_s e^2}{mc^2}\right)\mathbf{h} = 0, \tag{9}$$

which can also be written as

$$-\nabla^2 \mathbf{h} + \frac{1}{\lambda^2}\mathbf{h} = 0, \tag{10}$$

where

$$\lambda = \left(\frac{mc^2}{4\pi n_s e^2}\right)^{1/2} \tag{11}$$

has the units of length and is defined as the **London penetration depth**. For an infinite slab of superconductor filling the half-space $x > 0$, the one-dimensional form of Eq. (10) is given by

$$\frac{d^2}{dx^2}h(x) - \frac{1}{\lambda^2}h(x) = 0, \tag{12}$$

and the field inside the superconductor is given by

$$h(x) = H_a \exp(-x/\lambda), \tag{13}$$

where H_a is the field applied parallel to the superconductor surface. From Eq. (13) it is clear that deep within the SC (i.e. as $x \to \infty$) the microscopic field $h(x) \to 0$ and we

4

have the Meissner effect once again. The penetration depth, λ, is also the characteristic depth within which the screening currents flow in order to exclude the applied magnetic field. The superconducting current $\mathbf{J}$, in terms of the vector potential $\mathbf{A}$, is given by:

$$\mathbf{J}(\mathbf{r}) = -\frac{n_s e^2}{mc}\mathbf{A}(\mathbf{r}) = -\frac{c}{4\pi}\frac{1}{\lambda^2}\mathbf{A}(\mathbf{r}), \tag{14}$$

This equation is effectively "Ohm's Law" for a type-II superconductor and is another expression of the London equation.

Whilst the London equation is successful in describing the Meissner effect and providing a definition for the penetration depth, the equation is deficient in that: (i) it is a local theory and is not viable for a type-I superconductor in which the electrodynamics are non-local and (ii) it offers no explicit temperature dependence for the superconducting electron density, n_s.

For a more comprehensive treatment see Ref. [12] and references therein.

1.6 The Gorter-Casimir Temperature Dependence of λ

The two-fluid model proposed by Gorter and Casimir [11] in 1934 was successful in explaining some properties of superconductors. It is based on the assumption that the total electron density in the superconductor is given by $n=n_s+n_n$, where n_s and n_n are the superconducting and normal conduction electron densities, respectively.

An empirical form for the temperature dependence of the penetration depth λ is given by [13]:

$$\lambda(t) = \lambda_o(1 - t^4)^{-1/2}, \tag{15}$$

where $\lambda_o = \lambda(T = 0)$ and $t = T/T_c$ is the reduced temperature. Fig. 2 shows the variation of the reduced penetration depth, λ/λ_o, as a function of reduced temperature, t. It is clear that the penetration depth diverges close to the critical temperature, T_c.
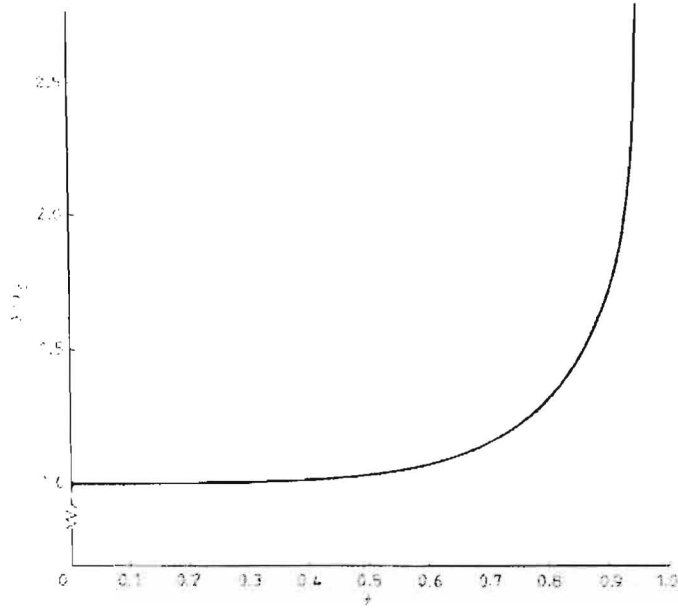
Fig. 2: Temperature dependence of the reduced London penetration depth, λ/λ_o (from Tilley [14]).

1.7 The Ginzburg-Landau Theory (1950)

The Ginzburg and Landau [15] (G-L) theory expresses the superconducting electron condensation in terms of a planar wave function of the form:

$$\psi(\vec{\mathbf{r}}) = \mid \psi \mid e^{i\varphi(\vec{\mathbf{r}})}, \tag{16}$$

where $\varphi(\vec{\mathbf{r}})$ and $\psi(\vec{\mathbf{r}})\psi^{\star}(\vec{\mathbf{r}}) = n_s(\vec{\mathbf{r}})$ are the phase and the superconducting electron density respectively at a point $\vec{\mathbf{r}}$. The superconductor free energy density is then expressed as an expansion in even powers of ψ, i.e. by [16]:

$$f_s = f_n + \underbrace{\alpha\mid\psi\mid^2 + \frac{\beta}{2}\mid\psi\mid^4}_{Potential\ Energy\ Term} + \underbrace{\frac{1}{2m^*}\left|\left(\frac{\hbar}{i}\nabla - \frac{e^*}{c}\mathbf{A}\right)\psi\right|^2}_{Kinetic\ Energy\ Term} + \underbrace{\frac{h^2}{8\pi}}_{Field\ Energy\ Term}, \tag{17}$$

where α and β are constants of the material, e^* and m^* are respectively the effective electron charge and mass.

6

Minimisation of Eq. (17) with respect to the order parameter ψ, and the vector potential $\mathbf{A}$, yield a pair of coupled equations (G-L equations) given by:

$$\alpha\psi + \beta|\,\psi\,|^2\psi + \frac{1}{2m^*}\left(\frac{\hbar}{i}\nabla - \frac{e^*}{c}\mathbf{A}\right)^2\psi = 0 \tag{18}$$

and

$$\mathbf{J} = \frac{c}{4\pi}\nabla\times\mathbf{h} = \frac{e^*\hbar}{2m^*i}\left(\psi^*\nabla\psi - \psi\nabla\psi^*\right) - \frac{e^{*2}}{m^*c}\psi^*\psi\mathbf{A}. \tag{19}$$

For a more detailed treatment see Refs. [16] and [17].

1.8 Implications of the G-L Equations

A summary of the implications of the G-L equations, outlined in greater detail in Refs. [18] and [19], is briefly presented here.

1.8.1 The Critical Field, $H_c(T)$

Setting $\mathbf{A} = 0$ in Eq. (18), gives two obvious solutions, namely: $\psi = 0$, which describes the normal state and $\psi = \psi_o$, which describes the superconducting state. With the assumption that the spatial variation of ψ is small, Eq. (18) reduces to:

$$|\,\psi_o\,|^2 = -\frac{\alpha}{\beta}, \tag{20}$$

where α and β are defined as:

$$\alpha = a\,(T - T_c) < 0 \tag{21}$$

$$\beta = \mathbf{constant} > 0, \tag{22}$$

where a is a positive constant, T and T_c are the actual and critical temperatures, respectively. The basic assumption of the model, namely: $n_s = |\,\psi_o\,|^2 \propto (T_c - T)$, implies that near T_c the superconducting electron density tends to zero, and the superconducting state is supressed.

7

The substitution of Eq. (20) into Eq. (17), together with $\mathbf{A} = 0$ and $\mathbf{h} = 0$, yields

$$f_s - f_n = -\frac{\alpha^2}{2\beta}. \tag{23}$$

A comparison of Eqs. (1) and (23) shows that $H_c{}^2/8\pi = \alpha^2/2\beta$

1.8.2 The Penetration Depth, $\lambda(T)$

For negligible spatial variation of the wave function, ψ, and considering small magnetic fields, Eq. (19) becomes:

$$\mathbf{J} = -\frac{e^{*2}|\psi_o|^2}{m^*c}\mathbf{A}. \tag{24}$$

Re-defining λ in the form:

$$\frac{1}{\lambda^2} = \frac{4\pi e^{*2}|\psi_o|^2}{m^*c^2}, \tag{25}$$

again yields the London equation [Eq. (14)]. The temperature dependence of the penetration depth is now given by: $\lambda(T) \propto (T_c - T)^{-1/2}$ near T_c and diverges as $T \to T_c$.

1.8.3 The Coherence Length, $\xi(T)$

The one-dimensional form of Eq. (18) with $\mathbf{A} = 0$, is:

$$-\frac{\hbar^2}{2m^*}\frac{d^2\psi}{dx^2} + \alpha\psi + \beta|\psi|^2\psi = 0. \tag{26}$$

This allows for the definition of a length $\xi(T)$, defined by

$$\xi^2(T) = \frac{\hbar^2}{2m^*|\alpha(T)|}, \tag{27}$$

known as the coherence length of the superconductor. This is the characteristic distance over which the order parameter, $\psi(\vec{\mathbf{r}})$, varies in the superconductor. The temperature dependence of the coherence length is given by: $\xi(T) \propto (T_c - T)^{-1/2}$ and diverges near T_c.

8

1.8.4   The Ginzburg-Landau Parameter, κ

The G-L parameter is defined by the relation $\kappa = \lambda/\xi$. Both λ and ξ vary approximately as $(T_c - T)^{-1/2}$ implying that κ is approximately independent of temperature (valid in the high κ limit).

1.9   Type-I and Type-II Superconductors

1.9.1   Type-I ($\kappa < 1/\sqrt{2}$)

Ginzburg and Landau solved the G-L equations [Eqs. (18) and (19)] for the case of $\kappa = \lambda/\xi < 1/\sqrt{2}$, which is descriptive of a pure type-I superconductor. The net superconductor/normal interfacial energy for this type of superconductor is determined by the negative and positive energy contributions respectively, from the decrease in energy resulting from the penetration of the magnetic field into the superconductor and the increase in energy from the resultant reduction of superconducting order in the superconducting region. The net superconductor/normal interfacial energy is given approximately, by:

$$\Delta E = \frac{1}{2}\mu_o H_c^2 (\xi - \lambda),\tag{28}$$

and is positive when the magnetic penetration depth λ is smaller than the coherence length ξ. See Ref. [20] for details.

A type-I superconductor of zero demagnetising coefficient exhibits perfect diamagnetism for the applied field in the range $0 \leq H_a \leq H_c$, for a zero-field cooled (ZFC) specimen, and then returns to the normal state for $H_a > H_c$ as illustrated in Fig. 3. [Note: $\mathbf{B} = 0$ so from $\mathbf{B} = H_a + 4\pi M$, $-4\pi M = H_a$]
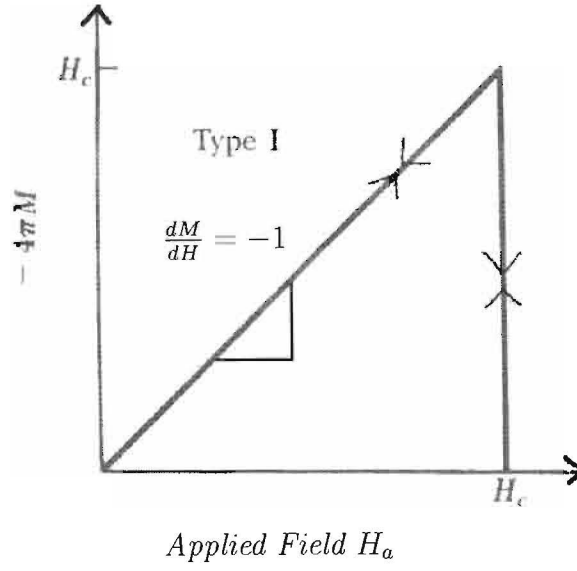
Fig. 3: Magnetisation curve for a type-I superconductor $(\kappa < 1/\sqrt{2})$, with zero demagnetising factor, i.e. a long cylinder in a parallel applied magnetic field H_a (From Kittel [21]).

1.9.2 Type-II $(\kappa > 1/\sqrt{2})$

The case $\kappa > 1/\sqrt{2}$, which describes type-II superconductors, was solved by Abrikosov [22] in 1957. In this case the superconductor/normal interfacial energy, given by Eq. (28), is negative.

A type-II SC (Fig. 4) has three critical fields, namely the lower critical field, H_{c1}, an upper critical field, H_{c2}, and H_c as defined by Eq. (1). For $H_a < H_{c1}$, for a zero-field cooled (ZFC) specimen, the superconductor exhibits perfect diamagnetism, and for $H_a > H_{c2}$, the superconducting phase is suppressed.

10
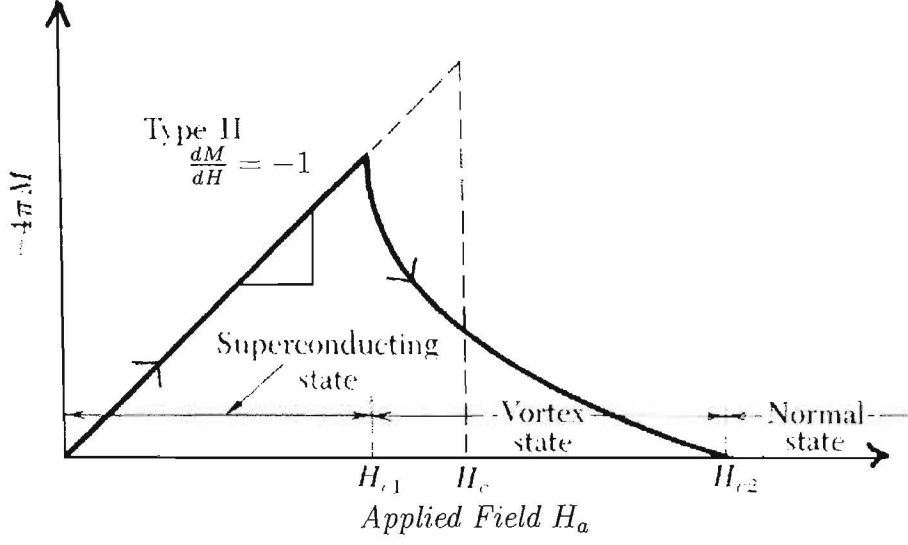
Fig. 4: Magnetisation curve for a type-II superconductor $\left(\kappa > 1/\sqrt{2}\right)$ with zero demagnetising factor (From Kittel [21]).

In the intermediate field range $H_{c1} \leq H_a \leq H_{c2}$, the superconductor is said to be in the *mixed* or *vortex* state where magnetic flux enters the bulk of the superconductor in the form of a 2-dimensional lattice (see Fig. 5) of singly quantized "vortices" (i.e. containing quantum of flux $\Phi = hc/2e$). Each vortex has a normal core region of radius ξ (the coherence length) and a circulating current that extends out to a distance λ (the magnetic penetration depth) from the center of the normal core. See Ref. [23] for details.

|— 1μm —|
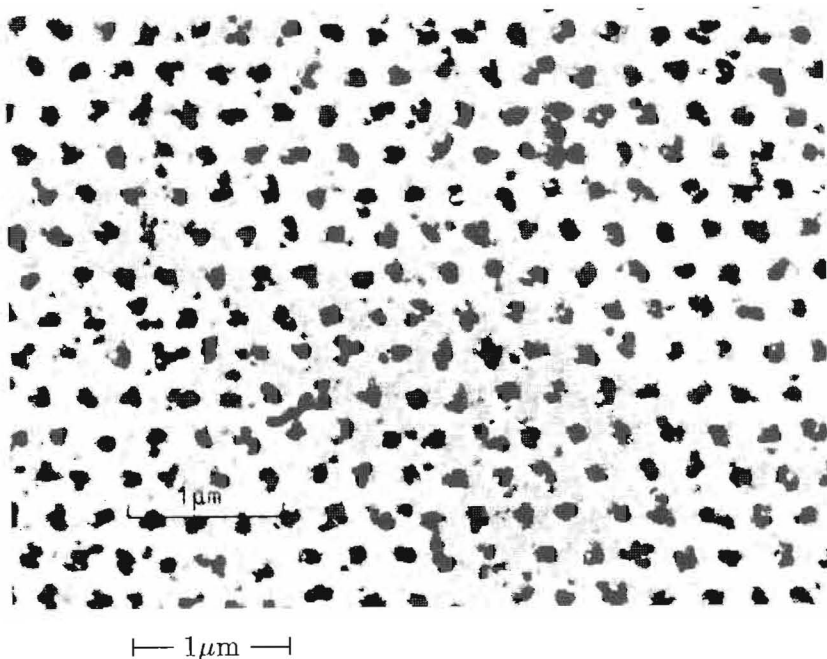
Fig. 5: An image of a 2-dimensional (triangular) array of vortices
(from Tilley) [24].

Ref. [21] gives a more detailed account of type-I and type-II superconductors.

1.10 BCS Theory (1957)

The BCS theory is a microscopic theory of superconductivity formulated by Bardeen,
Cooper, and Schriefer [25]. The theory is based on the idea that there is an attractive
interaction between pairs of electrons in the superconducting state. The coupled electron
pairs, known as Cooper-pairs, have equal and opposite momenta and spins and are sepa-
rated, on average and on overlap, by the coherence length ξ. Cooper-pairs are, therefore,
bosons and obey Bose-Einstein statistics. The pertinent aspects of the BCS theory, such
as the superconducting gap parameter $\Delta(T)$, the critical temperature T_c, the coherence
length $\xi(T)$, and the penetration depth $\lambda(T)$, will be briefly discussed here. See Ref. [25]
for a more detailed treatment.

1.10.1 BCS Superconducting Gap Parameter, $\Delta(T)$

BCS introduces a temperature dependent gap parameter, $\Delta(T)$, which is also referred to as the superconducting order parameter (equivalent to $\mid \psi \mid^2$ in the G-L Theory) and is given by:

$$\Delta(T) = 1.74\Delta(0)(1 - T/T_c)^{1/2}, \tag{29}$$

where $T \leq T_c$ and $\Delta(0)$ is given (in the weak-coupling limit) by:

$$\Delta(0) = \frac{3.52k_B T_c}{2}, \tag{30}$$

where k_B is Boltzmann's constant.

Fig. 6 shows the temperature dependence for the reduced energy gap parameter $\Delta(T)/\Delta(0)$. This temperature dependence is accurately followed in the weak-coupling limit, but remains a relatively good approximation in general.
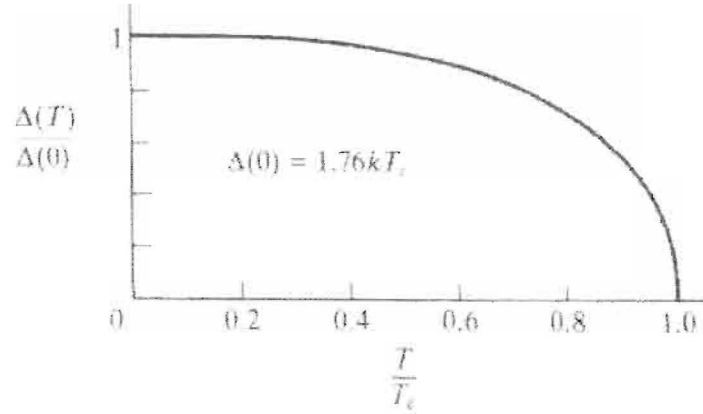
Fig. 6: Temperature dependence of the BCS reduced gap parameter, $\Delta/\Delta(0)$ (from Tinkham) [26].

1.10.2 BCS Critical Temperature, T_c

The critical temperature T_c of a superconductor, is, according to the BCS theory, given by:

$$T_c = \frac{1.13\hbar\Theta_D}{k_B} \exp(-1/\lambda_{ep}), \tag{31}$$

13

where Θ_D is the Debye temperature and λ_{ep}, a dimensionless electron-phonon coupling parameter, which is approximately 0.3 for conventional superconductors. For 100K$<$ Θ_D $<$500K, the BCS theory predicts a maximum T_c of around 25K.

1.10.3 BCS Coherence Length, $\xi(T)$

The BCS theory introduces a temperature-independent coherence length, ξ_o, given by:

$$\xi_o = 0.18 \frac{\hbar v_F}{k_B T_c}, \tag{32}$$

where v_F is the Fermi velocity. Taking $v_F = 10^6 \text{m.s}^{-1}$ and $T_c \approx 10\text{K}$, yields $\xi_o \sim 1800\text{Å}$. The relation between the temperature-dependant G-L coherence length, $\xi(T)$, and the temperature-independent BCS coherence length, ξ_o, is a direct consequence of the mean-free path, l_e, of the electrons. Two limits are considered, namely:

(i) the "clean-limit" $(l_e \gg \xi_o)$, which yields

$$\xi(T) = 0.74\xi_0 \left(\frac{T_c}{T_c - T} \right)^{1/2}, \tag{33}$$

and

(ii) the "dirty-limit" $(l_e \ll \xi_o)$, which yields

$$\xi(T) = 0.85\sqrt{\xi_o l_e} \left(\frac{T_c}{T_c - T} \right)^{1/2}. \tag{34}$$

1.10.4 BCS Penetration Depth, $\lambda(T)$

The BCS theory for the penetration depth gives [27]:

$$\lambda(T) = \lambda(0) \left[\frac{\Delta(T)}{\Delta(0)} \tanh \left(\frac{\Delta(T)}{2k_B T} \right) \right]^n, \tag{35}$$

where $n = -1/3$ for the "clean-limit" and $n = -1/2$ for the "dirty-limit".

1.11 Conventional and High-T_c Ceramic Superconductors

1.11.1 Conventional Superconductors

From the list of metallic elements, including Al, Pb, and Nb (all of which are classified as conventional superconductors), Nb has the highest T_c value of 9.2K and is the only type-II superconductor. Binary compounds including Nb_3Sn and Nb_3Ge, and the binary alloy Nb-Ti, are type-II superconductors and possess significantly higher critical temperatures than metallic elements. In particular, Nb_3Ge has the highest recorded T_c of 23K. In agreement with BCS Theory, no conventional superconductors have been found with $T_c > 25$K. See Ref. [28] for a detailed account of conventional superconductors.

Conventional metallic superconductors can be fabricated to have "granular" properties. Such a granular superconductor would consist of superconducting grains separated by an insulating layer of thickness of the order greater than the coherence length ξ. For example granular Al, in which Al grains are surrounded by Al_2O_3.

1.11.2 High-T_c Superconducting Ceramic Oxides

With the exception of $LiTi_2O_4$ and $Ba(PbBi)O_3$ (both with $T_c \approx 13$K), oxide superconductors were generally known to possess much lower critical temperatures [30]. It must, therefore, have been very surprising when the Ba-La-Cu-O system, with a critical temperature of approximately 30K, was discovered [4]. To date, an unprecedented amount of research has been conducted on a variety of oxide systems. A brief discussion on the characteristic features of these "high-T_c" superconducting oxides, namely: structure and chemistry, high critical temperature and short coherence length, will be briefly discussed here. For a more detailed account of high-T_c superconducting oxides see Ref. [31].

(i) Structure and Chemistry

Most high-T_c superconductors (HTSC) are layered perovskites, having the structure ABX_3. With a few exceptions, HTSC are mainly cuprates i.e. compounds containing copper in their structure. A fully oxygenated unit cell of $Y_1Ba_2Cu_3O_{6+x}$ (YBCO), with $x = 1.0$, is shown in Fig. 7. The unit cell is orthorhombic with lattice parameters of $a, b \sim 4$Å and $c \sim 12$Å. The superconducting carriers (holes) are known to be located predominantly in

the CuO_2 planes. Consequently $Y_1Ba_2Cu_3O_{6+x}$ exhibits superconducting properties that are highly anisotropic. The preferred current conducting direction is in the a-b (basal) plane, with the c-axis direction being relatively more weakly conducting [32].
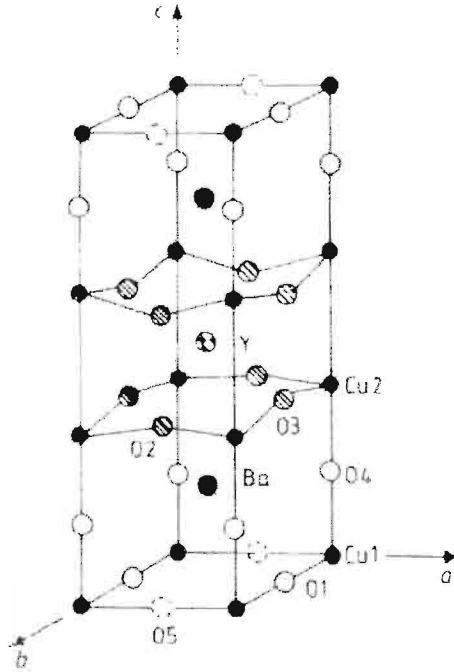
Fig. 7: Unit cell for superconducting $Y_1Ba_2Cu_3O_{6+x}$ ($x = 1.0$),
(from Kittel) [33].

The "partial oxygen content", x, in the formula $Y_1Ba_2Cu_3O_{6+x}$ determines the hole concentration in the CuO_2 planes. A non-superconducting tetragonal phase occurs for $0.0 < x < 0.4$, while a superconducting orthorhombic phase is obtained for $0.4 < x < 1.0$.

When oxygen is diffused into the oxygen deficient $Y_1Ba_2Cu_3O_{6+x}$ the oxygen goes into vacancy sites in the parallel Cu-O chains (along the b axis of Fig. 7). In order to maintain a net zero charge, electrons are removed from the CuO_2 planes, thereby creating "conduction" holes in the CuO_2 planes that are available to form Cooper-pairs when $T < T_c$.

The valence or charge state of the Cu atoms depend on the partial oxygen content. For example $Y_1Ba_2Cu_3O_6$, an insulator, contains Cu^{2+} ions in the CuO_2 planes and Cu^{3+}

16

ions in the Cu-O chains, while $Y_1Ba_2Cu_3O_7$, a superconductor, contains $Cu^{2.33+}$ ions [34] (assuming that charge is distributed equally between the Cu atoms).

(ii) High Critical Temperature

High-T_c materials possess critical temperatures that far exceed the BCS limit, extending beyond 150K [6] for certain systems. It must be stated, however, that the mechanism for high-T_c superconductivity is not yet fully understood. The onset critical temperatures T_c for $Y_1Ba_2Cu_3O_{7-x}$ and $Eu_1Ba_2Cu_3O_{7-x}$, which are materials used in the present investigation, are respectively approximately 91.5K and 93.7K [35].

The binding energy of the Cooper-pairs, $\triangle(0)$, is approximately 10meV at 100K. This value is about ten times greater than the binding energy of the Cooper-pairs in conventional superconductors, implying that the Cooper-pairs are more tightly bound in ceramic superconductors.

(iii) Short Coherence Length

The high-T_c materials (especially cuprates [36]) have very short coherence lengths (ξ is of the order of and less than 10 Å). This is expected from the BCS theory, which predicts $\xi \propto T_c^{-1}$. For YBCO: $\xi_{ab}(0) \sim 15$Å and $\xi_c(0) \sim 4$Å with $\lambda_{ab} \sim 1500$Å and $\lambda_c \sim 6000$Å. Thus $\kappa_{ab} = \lambda_{ab}/\xi_{ab} \simeq 100 \gg 1$, and YBCO is an extreme type-II superconductor. This short coherence length, of the order of the dimension of a unit cell, is partly responsible for the granular effects associated with these systems.

1.12   Grain Boundaries in High-T_c Superconductors

Polycrystalline specimens of high-T_c superconductors are prepared using a technique called **powder processing** (see Section 3.1). This technique includes a process called sintering, in which randomly oriented grains of the precursor material are effectively fused together. The "grain boundaries" (GB's) between these fused grains are 2-D interfacial defects that are roughly a few unit cells wide. See Ref. [37].

There are generally a number of types of grain boundaries, which include: tilt boundaries and twist boundaries. A tilt boundary usually occurs when two crystals are rotated through some angle with respect to each other about an axis that is parallel to the

grain boundary plane. When the angle of orientation is small, i.e. small atomic mismatch, the interfacial defect is called a "low-angle" grain boundary. The term high-angle grain boundary is used when the degree of mismatch becomes large. A twist boundary on the other hand occurs when two crystals are rotated, with respect to each other, through some angle that lies in the grain boundary plane i.e. the rotation axis is perpendicular to the grain boundary plane. Small angle tilt and twist boundaries are well described by standard theory for edge and screw dislocations respectively [38, 39].

A misorientation-dependant grain boundary energy arises as a consequence of the bonding along the grain boundaries, which deviates markedly from the typical bonding observed within individual grains. Consequently, GB's are found to be "more chemically reactive than the grains themselves" [40]. Also, impurity atoms diffuse away from or towards the GB's, and reduce the free energy of the grain boundary.

The inter-granular regions or grain boundaries in cuprate systems act as superconducting weak-links or tunnel junctions due to the short coherence length associated with these systems [36]. Granular behaviour (or short coherence length effects) are responsible [29] for the low transport critical current density obtained experimentally [41] in polycrystalline materials. Whenever the Josephson penetration depth λ_j (to be discussed in Section 1.13.2) is of the order and greater than the average grain diameter a_o, the weak-link is referred to as a "short" junction. This is appropriate in the present work and will be shown in Section 4.3.3.

1.13 Josephson Effects in High-T_c Superconductors

B.D Josephson (1962) accurately predicted that a current of Cooper-pairs had the ability to quantum mechanically tunnel through a thin insulating layer sandwiched between two single superconductors. He also predicted that this current would be able to flow without any resistance. The junction, however, has a maximum current associated with it, beyond which enough energy is supplied to the Cooper-pairs to cause them to break-up into single electron/hole (excitons) and, thereafter, the current flows with some non-zero resistance, and a small voltage develops across the junction. The direct current (d.c) Josephson effect for an ideal, uniform junction will be reviewed here in Section 1.13.1 below. Later, in Section 2.4, non-ideal junctions, which are more descriptive of the grain boundary

18

junctions of the specimens used in the present work, will be reviewed. The Josephson effect is reviewed in detail in Refs. [42] and [43].

1.13.1 D.C Josephson Effect for an Ideal Junction

Consider two single superconductors, S_1 and S_2, with planar-wave order parameters $\Psi_1 = \mid \Psi_1 \mid e^{i\phi_1}$ and $\Psi_2 = \mid \Psi_2 \mid e^{i\phi_2}$ respectively, where ϕ_1 and ϕ_2 are the respective phases. Josephson showed that the superconducting current through the junction is proportional to the phase difference between the two superconductors, and is given by:

$$I = I_o \sin(\phi_2 - \phi_1), \tag{36}$$

where I_o is the maximum current that can flow through the junction. Ambegaokar and Baratoff (AB) [44] have given an expression for I_o for an ideal planar S-I-S (Superconductor-Insulator-Superconductor) junction, namely:

$$I_o = \frac{\pi \triangle(T)}{2e R_n} \tanh\left[\frac{2\triangle(T)}{2k_B T}\right] \tag{37}$$

where $\triangle(T)$ is the temperature dependant gap parameter and R_n is the normal state resistance. The critical current, I_o, is strongly influenced by the magnetic field induction B in the junction, and becomes zero whenever the total flux, Φ, threading the junction is an integral multiple of the flux quantum, $\Phi_o = hc/2e$. The relation [Eq. (37)] for I_o as a function of Φ/Φ_o is shown in Fig. 8. This result is equivalent to the "Fraunhofer diffraction pattern" (intensity as a function of angle) observed for a single-slit.
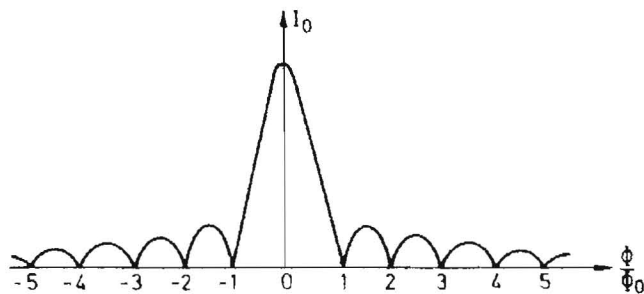
Fig. 8: Critical current I_o for a single ideal Josephson-junction
as a function of total flux Φ/Φ_o (from Cyrot [45]).

Polycrystalline high-T_c ceramics consist essentially of a 3D array of randomly oriented grains of random size. This results in an averaging out of the "Fraunhofer diffraction pattern" observed for an ideal junction (Fig. 8) and the expression for I_o, given by Eq. (37), is not directly applicable [46]. The detailed treatment of a random array of random Josephson-junctions will be given in Section 2.4.

1.13.2 The Josephson Penetration Depth, λ_j

The assumption of a non-uniform field across the junction, leads to the result that the junction also exhibits a partial Meissner effect. For small magnetic fields, a Josephson current has the tendency to "screen" the magnetic field from the junction. Consequently there exists a characteristic length for field variation within the junction. This is called the Josephson penetration depth, λ_j, and is given by [47]:

$$\lambda_j = \left[\frac{c\Phi_o}{4\pi^2 a_o J_o \mu_e}\right]^{1/2},\tag{38}$$

where J_o is the Josephson current density, and μ_e is the effective permeability.

1.13.3 The Josephson Coupling Energy, E_j

The Josephson coupling energy, E_j, is given by:

$$E_j = \frac{\hbar}{2e}I_o = \Phi_o I_o,\tag{39}$$

This energy must be sufficiently high to maintain phase coherence across the junction.

20

2 LITERATURE SURVEY

The Weak-Link Problem in Granular High-T_c Superconductors

2.1 Introduction

The high-T_c superconductor systems are highly anisotropic layered perovskite materials (see Section 1.11.2). This fact alone is, however, not responsible for the low current carrying capabilities of polycrystalline specimens. Single crystal [48] and thin film [49] specimens of YBCO have critical current densities in excess of 10^6 A.cm^{-2} at 4.2K.

The bulk-sintered polycrystalline YBCO specimens of Ekin *et al.* [50], however, exhibit transport critical current densities of approximately two orders of magnitude smaller than the theoretical expectation. The critical currents also decreased very rapidly in small ($\sim$ mT) to moderate magnetic fields. This behaviour is a consequence of the "weak-link" behaviour of the grain boundaries in bulk-sintered polycrystalline superconductors.

The "weak-link" behaviour is a result of very short coherence length, ξ, which is of the same order as the unit cell dimension and much smaller than the length scale of crystalline inhomogeneities. Order parameter, and hence critical current density, suppression occurs in the grain boundary "weak-link".

Although critical current densities in "bulk-sintered" superconductors are lower than expected, the manufacture of specimens of a specific geometry for a wide range of applications, using this technique, has its advantages [51]. It is, therefore, of technological importance that the weak-link behaviour, in bulk-sintered materials, be understood and improved.

Properties of single grain boundary weak-links in bicrystals and epitaxial thin films will be reviewed in Section 2.2. The technique of doping, which is successful in improving weak-link behaviour in bulk sintered polycrystalline materials, will be also be reviewed. The literature survey also extends to the behaviour of a network of weak-links in polycrystalline materials and the chapter closes with a brief outline of the approach to be adopted in the present investigation.

2.2   Properties and Characteristics of Weak-links

Here the properties of single weak-links in bicrystals and in epitaxial thin films will be reviewed.

2.2.1   Magnetic Field Dependance of the Critical Current Density

This Section contains a brief summary of an investigation by Yanson [52] on the "Effect of Fluctuations on the Dependence of the Josephson Current on the Magnetic Field". The investigation considers the effect of inhomogeneities, in the oxide layer of non-ideal single Sn-oxide-Sn Josephson tunnel junctions, which lead to extraordinary $I_c(H)/I_o$ behaviour. Here $I_c(H)$ and I_o are, respectively, the field-dependent Josephson critical current and zero-field critical current. For H increasing continuously, the minima of the oscillating Josephson critical current have a non-zero value. The amplitude of the average Josephson critical current is a rapidly decreasing function of H and asymptotically approaches some value of I_o. The presence of inhomogeneities in the oxide layer causes the critical current to be spatially variant inside the junction. These so-called "random fluctuations" result in the loss of the typical "Fraunhofer diffraction" pattern expected for uniform Josephson tunnel junctions (see Fig. 8).

Experiments on epitaxial thin films of YBCO with single grain boundaries also show very anomalous $J_c(B)$ behaviour, suggesting that these grain boundaries are also irregular or non-uniform and consist of areas of strong and weak (spatially varying) Josephson coupling behaviour [53].

The $J_c(B)$ behaviour reported elsewhere, for polycrystalline superconductors, also show a degradation of the "Fraunhofer diffraction pattern" [41, 46, 54, 55]. Apart from spatial inhomogeneities or random fluctuations occuring within individual Josephson-junctions in polycrystalline ceramic materials, it is necessary to include the effects of random orientations and dimensions of the junctions. These combined effects result in quite a complicated percolation problem.

2.2.2 Orientation Dependance of the Critical Current Density

Critical current densities across grain boundaries, as a function of grain misorientation in the basal (a-b) plane, have been thoroughly investigated by Dimos and co-workers [56]. By creating almost c-axis aligned YBCO bicrystals, by the epitaxial growth of thin films on $SrTiO_3$ substrates, they observe that the ratio of the grain boundary critical current density $(J_c{}^{GB})$ to the average value of the individual grains $(J_c{}^{G})$ (i) is roughly inversely proportional to the misorientation angle, θ, for small θ $(0 - 20^o)$, and (ii) that it "saturates" at approximately 1/50 of the zero angle value for θ approximately equal to 20°.

2.2.3 Temperature Dependance of the Critical Current Density

The Ambegaokar-Baratoff temperature dependence for the critical current through a S-I-S Josephson-junction [Eq. (37)] gives a reasonably good fit to the experimental data of Mannhart *et al.* even though no insulating layer could be detected [58]. It was pointed out [58] that this temperature dependence of the critical current can also be used for dirty S-N-S junctions, provided that the occurrence of any notable phase change is confined to the normal layer. It is mentioned elsewhere [59] that a S-N-S junction, having an adequately thin normal layer, may display a critical current temperature dependence that is typical of a S-I-S Josephson-junction.

Other work reveals that the temperature dependence of the critical current density of ceramics is determined by the specimen morphology [61, 60]. Based on the particular annealing (in air or oxygen) temperature and conditions, a variety of temperatures dependences for the critical current, ranging from quadratic to the classical Josephson tunelling, can be obtained.

The temperature dependence of the grain boundary critical current density was also investigated (see Ref. [57] and references therein) for a grain boundary with misorientations of $\theta = 5^o$ and $\phi = 9^o$ in the basal-plane and between c-axes respectively. Below 30K, the grain boundary displays a slower temperature dependence than the individual grains. The temperature dependence of the grain boundary critical current density becomes more significant between 30 and 70K in YBCO. Close to the critical temperature, T_c, though,

23

the critical current densities of both the grain boundaries and the individual grains follow a power law dependence on temperature. "Spatial inhomogeneities" in the specimen are believed to be responsible for the behaviour close to T_c.

2.2.4 Current-Voltage Characteristics

Here we review the work of Dimos and co-workers [57], in particular the magnetic field and temperature dependence of the grain boundary current-voltage curves (CVC's). These curves exhibit a sudden, almost step-like, changeover, particularly at low temperatures, from zero-voltage across the grain boundary ($J < J_o$, where J_o is the maximum zero-voltage Josephson current density) to some non-zero voltage. For current densities exceeding J_o, the normal state resistance remains fairly constant, up to a few millivolts, for some GB's and up to as high as 75mV for other boundaries.

An investigation of the magnetic-field dependence of the CVC's conducted on YBCO bicrystals at 4.2K shows a very rapid decrease of the critical current with field up to approximately 360 Oe [57]. However, for magnetic fields in excess of 360 Oe the critical current increases with field and reaches a maximum value at 650 Oe where there appears to be an onset of resistive noise. Beyond 650 Oe, and up to about 1000 Oe, the grain boundary critical current density is found to be independent of magnetic field.

2.2.5 Direct Study of Individual Boundaries

With the aid of energy-dispersive x-ray analysis, in a scanning transmission electron microscope, localised (nm) composition changes both parallel and perpendicular to grain boundaries (in bulk-sintered YBCO) "free of second phase and structural defects" has been investigated by Babcock and Larbalestier [62]. The compositional profiles taken *perpendicular* to the grain boundaries reveal that the boundaries have an increased copper concentration and a reduced oxygen concentration. The "regular oscillatory" pattern of the concentration changes *along* the grain boundaries is believed to be a grain boundary characteristic. It is also believed that these variations in composition may be responsible for effectively reducing the grain boundary area, thus limiting the transport critical current flowing through them [62].

2.2.6 Morphology Dependance

The critical state model of Doyle and Doyle [61], which is specifically formulated for a random array of weak-link Josephson-junctions, has been used to study the effect of specimen morphology on properties of weak-links in bulk (untextured) sintered polycrystalline YBCO. Their investigation shows that the grain boundary normal state resistance decreases with average grain size, while other grain boundary specific parameters such as the $I_c R_n$ product and the maximum zero-field current density, J_{co}, increases with average grain size. These findings provide evidence that grain boundary weak-link properties are strongly dependent on specimen morphology.

2.3 Chemical Doping in Polycrystalline Superconducting Ceramic Oxides

The effect of silver doping on polycrystalline $Y_1 Ba_2 Cu_3 O_{7-x}$ was investigated by Jung et al. [63]. They report that the addition of silver, either as an oxide powder or metal, prior to the sintering process, results (i) in silver occupying voids in the ceramic material and (ii) the grain boundary junctions being coated with silver. Silver doping, 10 wt.% composition, improves the zero-field inter-granular critical current, in comparison to the undoped specimen, by a factor of three at 77K.

The influence of silver doping on grain boundary weak-link properties was investigated by Jarvis and Doyle [64] using a critical state model [65] containing grain boundary specific parameters. Their results clarify and confirm results established elsewhere (see [64] and references therein).

Jin et al. [66] investigate the effect of Sb_2O_3 doping on polycrystalline YBCO. Zero-field transport current density, measured using the standard four-probe technique at 77K, improved by a factor of 3-6 for 0.5 wt.% Sb_2O_3 doping, and by a factor of 3 for 2 wt.% Sb_2O_3 doping. At 200 Oe, for 0.5 wt.% Sb_2O_3 doping, the critical current shows a 25-80 fold increase in comparison with an undoped specimen. The reduced field dependence of the transport J_c, for their specimens, was thought to be due to an appreciable improvement of weak-link behaviour as a result of Sb_2O_3 doping. The authors suggest that the improvement in the transport J_c is due to better coupling at "high-angle grain bound-

aries".

2.4 Weak-link Behaviour in Polycrystalline Superconductors

We will now review the paper by Meilikhov and Doyle [65] on the "Universal Magnetic Field Dependence of the Inter-granular Critical Current Density in High-Tc Ceramic Superconductors", which gives a theoretical justification of an empirical model by Doyle [61].

The magnetic field dependence of the critical, i_{cB}, for single Josephson-junction with a spatially random current distribution is given by [52]:

$$\frac{i_{cB}}{i_c(0)} = \left[\left(\frac{\sin b}{b} \right)^2 I_1^2(b) + \left(\frac{\cos b}{b} \right)^2 I_2^2(b) \right]^{1/2}, \tag{40}$$

where $b = 2\pi\lambda_g a_o B/\phi_o$ is the 'dimensionless' reduced flux in the junction, and a_o is the lateral dimension (perpendicular to the magnetic field) of the interlayer (the grain size in the present work).

Expressions for $I_1^2(b)$ and $I_2^2(b)$ are given by:

$$I_1^2(b) = 1 + 2\gamma^2 \left[\sum_{n=1}^\infty \alpha_n^2 - \frac{1 - \exp(-2\pi f)}{\pi f} \left(\sum_{n=1}^\infty \beta_n \right)^2 \right]$$

and

$$I_2^2(b) = 2\gamma^2 \left[\sum_{n=1}^\infty \alpha^2_{n-1/2} - \frac{1 + \exp(-2\pi f)}{\pi f} \left(\sum_{n=1}^\infty \beta_{n-1/2} \right)^2 \right],$$

where $\alpha_n^2 = \left[\frac{b^2}{b^2 - \pi^2 n^2} \right]^2 \frac{1}{1 + n^2/f^2}$, $\beta_n = \left[\frac{b^2}{b^2 - \pi^2 n^2} \right] \frac{1}{1 + n^2/f^2}$, $f = 1/2\pi \left(a_o/r_o \right)$ and

$\pi f \gamma^2 = \overline{(j_c - \bar{j}_c)}^2 / (\bar{j}_c)^2$. Here j_c and $\bar{j}_c$ are the local and mean critical current densities in the junction, and r_o is the correlation radius of the junction irregularities, which are related by the auto-correlation function:

$$\overline{\left[j_c(x_1) - \bar{j}_c \right]\left[j_c(x_2) \right]} = \overline{\left(j_c - \bar{j}_c \right)^2} \exp\left(\frac{-\mid x_1 - x_2 \mid}{r_o} \right), \tag{41}$$

26

where x_1 and x_2 are points in the plane of the grain boundary junction.

Note: f is a function of the correlation radius of spatial inhomogeneities (in the junction) which are responsible for fluctuations in the critical current, and γ, together with f, gives an indication of the extent of the variation of the critical current due to these inhomogeneities. Meilikhov [67] points out that a large value of the so-called "modulation-index", $\gamma(2\pi f)^{1/2}$, is obtained for a highly non-uniform spatial distribution of the critical current.

The critical current distribution function $f(i_c)$, is given from the percolation model, by:

$$f(i_c) = \begin{cases} const\big[i_c\big]^n, & i_c \leq i_o \\ 0, & i_c \geq i_o. \end{cases} \tag{42}$$

In order to estimate the critical current in a polycrystalline material consisting of superconducting grains connected by weak-link Josephson-junctions, a 3D array of junctions with $i_c > i^*$, where i^* is some minimum value, is considered. If the fraction of such junctions

$$P(i^*) = \int_{i^*}^{\infty} f(i_c)di_c = 1 - \int_0^{i^*} f(i_c)di_c, \tag{43}$$

exceeds the percolation limit P_c, this constitutes an infinite cluster of junctions which provide percolation of the superconducting currents through the entire system. The network critical current i_{cB}, is limited by the "weakest links" having the lowest critical current i^*. Thus i_{cB} is given by

$$i_{cB} = const(P - P_c)^t i^*(P), \tag{44}$$

where t is the critical conductivity index. For various possible percolation lattices, the values of P_c $(0.25 < P_c < 0.6)$ and t $(1.0 < t < 1.5)$ do not significantly influence the final result of the model.

The magnetic field dependence of the distribution function $f(i_c)$ is now taken into consideration. For square junctions (side a) having random orientations, a modified distribution function

$$f_B(i_{cB}) = \frac{2}{\pi} \int_0^{\pi/2} f\{i_c[i_{cB}(b\sin\varphi)]\} \left| \frac{\partial i_c}{\partial i_{cB}(b\sin\varphi)} \right| d\varphi, \qquad (45)$$

is obtained. Here φ is the angle between the junction plane and the direction of the magnetic field.

The distribution function, Eq. (42), is now substituted into Eq. (45) and the modified distribution is determined. This modified distribution is then substituted into Eq. (43) to obtain $i^*(P)$ (the inverse of $P(i^*)$) and the critical current J_c is obtained by a maximization of Eq. (44). This yields an expression for J_c of the form,

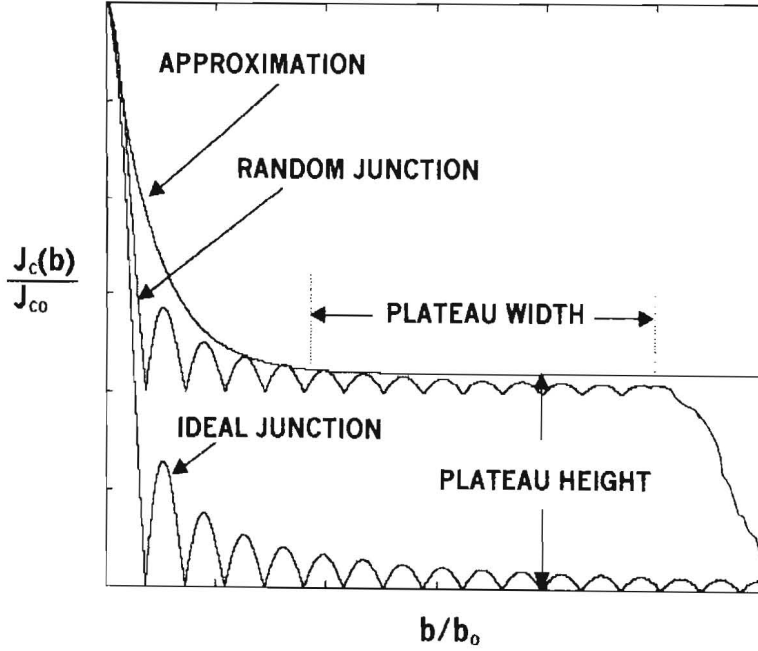$$J_c(b) \approx J_{co} A \left[\exp\left(b/b_o\right)^m + C \right]. \qquad (46)$$

Fig. 9: The magnetic field dependence of the critical current density for an ideal junction, a random junction, and the approximation [Eq. (46) (with $m = 1$) - valid from $b = 0$ to the end of the plateau region].

28

Comparison with experiment [65] yields $m \cong 1$ in Eq. (46) and hence also Doyle's empirical expression [61]:

$$J_c(H) = J_{co}A\left[\exp(-H/H_o) + \delta\right], \tag{47}$$

where $J_{co} \equiv J_c(H = 0, T)$, $H_o = H_o(T)$, and $\delta = \delta(T)$ are characteristics of the weak-link network.

Fig. 9 is a plot of $J_c(b)/J_{co}$ versus b/b_o for an ideal junction, a random junction, and the approximation given by Eq. (46) (with $m = 1$ - valid only from $b = 0$ to the end of the plateau). Note that the detailed treatment relates the parameter f to the plateau width and the parameter γ to the height of the plateau.

Eq. (47) may be re-written in the form:

$$J_c(H, T) = J_0(T)\left[\exp(-H/H_o)\right] + J_1(T), \tag{48}$$

where $J_0(T) = J_{co}$ and $J_1(T) = J_0(T)\delta$ are the field-dependant and field-independent components respectively. [Note that A has been set equal to 1.]

The δ parameter used here has the same meaning as the γ parameter used by Meilikhov [67]. The δ parameter allows for the determination of the height of the plateau since δ, in the regime of interest, is just the ratio of the plateau critical current density to the zero-field critical current density [52, 67]. This dimensionless parameter can be expressed [68] as:

$$\delta \approx \left[\frac{2r_o}{a_o}\overline{(j_c - \bar{j}_c)}^2/(\bar{j}_c)^2\right]^{1/2}, \tag{49}$$

or

$$\delta \approx \left[\frac{2r_o}{a_o}\right]^{1/2}\psi, \tag{50}$$

where a_o is the average grain diameter, $\psi \equiv \left[\overline{(j_c - \bar{j}_c)}^2/(\bar{j}_c)^2\right]^{1/2}$ is the root-mean-squared

(r.m.s) fluctuation of the critical current density that occurs throughout the junction as a result of random spatial inhomogeneities (structural fluctuations), and r_o is the correlation radius for the r.m.s fluctuation in critical current density. The correlation radius r_o is determined by the autocorrelation function given by Eq. (41).

The temperature dependence of δ depends (in some complex way) on the morphology and chemical stoichiometry of the grain boundary junctions [70]. The temperature dependence of δ will also depend on the charge state of the Cu atoms in the Cu-O chain, which correspondingly depends on the oxygen content in the unit cell (see section 1.11.2 for details) in the grain boundary.

In addition to making possible a direct study of weak-link behaviour in polycrystalline ceramic superconductors, the model for the critical current density, given by Eq. (47), is able to account for the observed low field magnetisation behaviour. We now review the work by Doyle and Doyle [61] which describes how theoretical expressions for specimen magnetisation, obtained using the critical state equation, given below by Eq. (51), and the expression for the critical current density, given by Eq. (47), obtained from a percolation model [65], are fitted to experimental isothermal magnetisation data to yield values for the weak-link parameters.

These authors assume a long cylindrical specimen, of radius R, zero-field cooled and then subjected to a parallel applied field, H_a, which varies monotonically over the field range $0 \leq H_a \leq H_{c1g}$, where H_{c1g} is the field of the first penetration of the Abrikosov fluxons into the intra-granular material.

For applied fields in excess of $H_{c1j} < H_a < H_{c1g}$, where H_{c1j} is the field of the first penetration of the Josephson fluxons into the inter-granular material, a combination of current loops flowing through percolative networks of phase coherent coupled grains extending azimuthally around the specimen, as well as small loops around clusters of diversely coupled grains, oppose the penetration of Josephson fluxons into the inter-granular material. A radial flux gradient, into the specimen, with an associated macroscopic critical shielding current results.

Assuming a cylindrically symmetric local mean internal field $H(r)$ parallel to H_a, the radial field gradient is given by the critical state equation (in cylindrical geometry), namely:

$$\frac{dH}{dr} = \pm \left[\frac{4\pi}{c}\right] J_c(H,T), \tag{51}$$

where $J_c(H,T)$ is the local effective shielding or transport current density and is a single valued function of H for H_a increasing monotonically. The specimen magnetisation is then given by the expression

$$-4\pi M = H_a - \frac{2\mu_e}{R^2} \int_0^R H(r) r dr, \tag{52}$$

where $\mu_e = \mu_e(T) \equiv B/H$ is an effective permeability (see later).

In order to obtain an explicit expression for $M(H_a,T)$ using Eqs. (51) and (52), explicit expressions for $\mu_e(T)$ and $J_c(H,T)$ are required.

The expression for $J_c(H,T)$, given by Eq. (47), is substituted into Eq. (51) and integrated to obtain the mean internal field

$$H(r) = H_o \ln r \left[(1 + \delta\alpha)e^{-\epsilon(1 - \frac{r}{R})} - 1\right]/\delta, \tag{53}$$

where R is the specimen radius, $\alpha = \exp(-H_a/H_o)$, $\epsilon = (4\pi/c)\delta A J_{co} R/H_o$ and $\delta = J_1/J_0$ [See Eq.(48)]. The reduced flux front penetration distance x_o into the specimen, defined as $x_o = 1 - r_o/R$, where r_o is the flux front penetration radius, is given by

$$x_o = \frac{1}{\epsilon} \ln\left[\frac{1 + \alpha\delta}{1 + \delta}\right]. \tag{54}$$

Eq. (53) is then substituted into Eq. (52) and integrated by parts to yield, for $x_o \leq 1$,

$$-4\pi M = H_o\left[\frac{\epsilon}{6}[1 - (1 - x_o)^3] + \frac{1}{\epsilon^2}\left|\sum_{k=0}^{\infty} Q_k z^{2+2k} + 2\Omega \sum_{k=0}^{\infty} R_k z^{1+2k} - \Omega^2 \ln(\sinh z)\right|_{z=\ln(1+\delta)}^{z=\Omega+\delta}\right]$$

$$+ H_a[1 - \mu_e], \tag{55}$$

and, for $x_o \geq 1$,

$$-4\pi M = H_o \left[\frac{\epsilon}{6} + \frac{1}{\epsilon^2} \left| \sum_{k=0}^{\infty} Q_k z^{2+2k} + 2\Omega \sum_{k=0}^{\infty} R_k z^{1+2k} - \Omega^2 \ln(\sinh z) \right|_{z=\Omega}^{z=\Omega+\epsilon} \right]$$

$$+ H_a[1 - \mu_e], \tag{56}$$

where $\Omega = \ln(1 + \delta\alpha) - \epsilon$, $Q_k = 2^{2k} B_{2k}/(2 + 2k)(2k)!$, and $R_k = 2^{2k} B_{2k}/(2k + 1)!$, and B_{2k} are the Bernoulli numbers. Eqs. (55) and (56) are valid for all $\mid z \mid \leq \pi$ and the series converges sufficiently with $k = 4$. Eqs. (55) and (56) are then fitted to the experimental isothermal magnetisation curves, $M(H_a)$, with $J_{co}(T)$, $\delta(T)$, $H_o(T)$ and $\mu_e(T)$ as free fitting parameters.

2.5 Present Work

Meilikhov [68] has suggested that the appropriate manipulation of the chemistry of the inter-granular weak-link may possibly result in the attainment of higher critical current densities. It has been suggested by Mannhart *et al.* [58] that this could be achieved by the doping of the grain boundaries.

The present work, therefore, involves the experimental investigation of weak-link behaviour in a specimen comprising of a mixture of two control compounds namely: $Y_1Ba_2Cu_3O_{6+x}$ (YBCO) and $Eu_1Ba_2Cu_3O_{6+x}$ (EBCO), which are chemically and physically very similar and are both superconducting. It is expected that Yttrium (Y) and Europium (Eu) in the grain boundaries of the mixed specimen (C2MIX) will arrange during the solidification process to reduce the grain boundary energy, since the grain boundaries are "chemically more reactive than the individual grains" [69]. We believe that any improvement in the weak-link behaviour of the C2MIX specimen should result in higher field-independent critical current densities.

The investigation has been carried out using the consideration given in Section 2.4, where the inter-granular critical current density, obtained from a percolation model, is defined in terms of grain boundary weak-link parameters. This provides us with a "diagnostic tool" for investigating and detecting any structural changes that may occur in the grain boundaries of the C2MIX specimen, as compared with the two control specimens. Consideration of grain size and distribution should be taken into account.

3 EXPERIMENTAL

3.1 Introduction

The precursor superconducting ceramic oxide powders, namely: $Y_1Ba_2Cu_3O_{7-x}$ (YBCO) and $Eu_1Ba_2Cu_3O_{7-x}$ (EBCO), used in the present investigation, were purchased from Seattle Ceramic Specialists, Inc. (USA). Their X-ray diffraction analysis shows that the powders are single phase. Particle sizes are in the range $3-8\mu m$.

A technique known as **powder processing**, which entails the compacting of the powder into some specific shape by the application of pressure, was performed each specimen. After uniaxial powder processing, the pellets were sintered by exposing them to a sufficiently high sub-melting point temperature (approximately 1100^oC). During the sintering process neighbouring grains form into coherent grain boundaries and the density of the material increases. For a review of powder processing and sintering, see Ref. [72].

3.2 Specimen Preparation

3.2.1 Procedure for the Control Specimens

Approximately 1 gram of YBCO and 1 gram of EBCO were each weighed and individually pelletised at a pressure of 37Mpa for a period of 30 minutes. The final disc specimens had a diameter of approximately 13mm and thickness $\sim 2.5mm$. Each disc was thereafter placed in a ceramic crucible and annealed in accordance with the program given in Fig. 10. Several researchers [73, 74, 75, 76], working on EBCO, have annealed their specimens at temperatures ranging from 930 - 950^oC, some choosing to perform the sintering in a pure oxygen atmosphere [74, 75, 76]. Work done on YBCO indicate that favorable sintering temperatures range between 925 and 950^oC (for several hours) [41, 60, 71, 77].

The furnace was pre-heated to 940^oC. The control specimens were thereafter placed in the furnace and sintered at T_x=940^oC for 12 hours in flowing oxygen for the full duration of the heat treatment (see Fig. 10). The specimens were then cooled at a rate of 1^oC/min to 600^oC, held at this temperature for 2 hours before being cooled at a rate of 1^oC/min to 350^oC, held at this temperature for 8 hours before being cooled to room at a rate of 0.5^oC/min temperature. The sintered pellets were then weighed and their

diameters and thicknesses were measured. The respective densities (g/cc) of the YBCO and EBCO specimens were then calculated. Rod specimens were then cut from the discs with dimensions $10.6 \times 1.5 \times 1.5$mm with the aid of a diamond saw. Results are listed in Table 1.
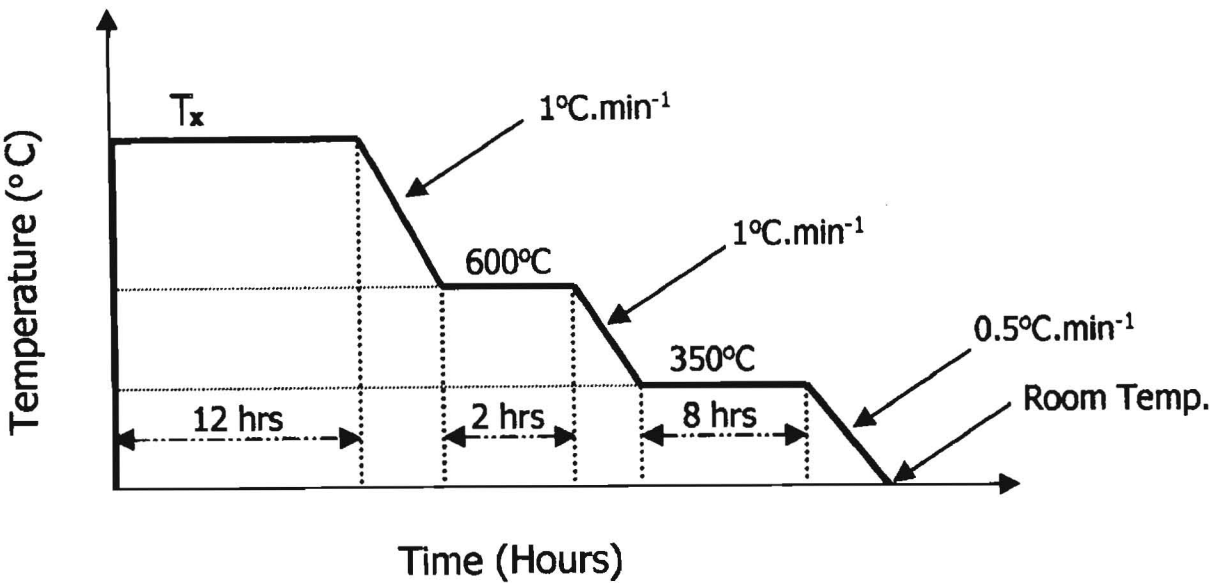

Fig. 10: Sintering and annealing program used for
the control specimens YBCO and EBCO,
and the mixed specimen C2MIX.

3.2.2 Procedure for the Mixed Specimen

Approximately 1 gram of YBCO and 1 gram of EBCO were put into a mixing container, which was put into a shaker inside the glove box. Mixing and shaking was carried out in an atmosphere of nitrogen gas. [Note that in usual practice the standard procedure is to perform the important stages of specimen preparation process, such as the grinding and mixing, in air]. Mixing was allowed to continue for a 30 minute period, yielding approximately 2 grams of the mixed precursor powder. Approximately 1 gram of the mixed precursor powder was then weighed and pelletised, at a pressure of 37Mpa for a period of 30 minutes, into a disc with a diameter of approximately 13mm and thickness ~ 2.5mm to yield specimen C2MIX.

34

The C2MIX specimen was then subjected to almost the same heat treatment (Fig. 10) used for the control specimens, except that the sintering was performed at T_x=950°C (furnace was pre-heated to 950°C). (Note: A suite of mixed specimens were made, with sintering temperatures ranging from 915 to 950°C. However, at the time of compilation of this thesis, the C2MIX specimen was the only mixed specimen for which the magnetisation data was complete. The effect of sintering temperature on weak-link properties is of obvious importance, but was considered to be beyond the scope of the present work and will be the subject of a future study.

Upon completion of the heat treatment, the sintered C2MIX pellet was weighed, its diameter and thickness was measured, and its density was determined (see Table 1). With the aid of the diamond saw, the specimen was cut into a rectangular bar of dimensions $10.6 \times 1.5 \times 1.5$mm.

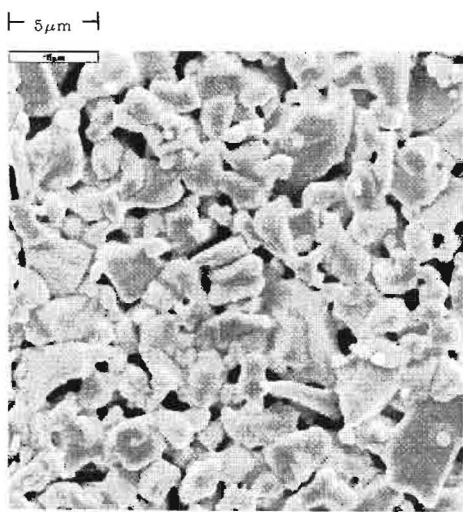|	Specimens		
Results	YBCO	EBCO	C2MIX
Mass of Disc (g)	0.9592	1.0154	1.3323
Diameter of Disc (mm)	11.42	11.10	10.70
Thickness of Disc (mm)	1.98	2.00	2.50
Density of Disc (g/cc)	4.73	5.23	5.93
Theoretical Max. Density (g/cc)	6.34	6.8	-
Dimensions of rect. bars (mm³)	$10.6\times1.5\times1.5$	$10.6\times1.5\times1.5$	$10.6\times1.5\times1.5$

Table 1: Tabulation of measurements performed on each specimen, after heat treatment.

3.3 Specimen Characterization
Scanning Electron Microscopy (S.E.M)

Scanning Electron Microscopy (S.E.M) was performed on off-cut remains from the disc specimens after the rectangular bars had been cut. S.E.M (5000X) was done on the cut faces, and the middle and the outer edge of each piece of specimen. A lower magnification (1500X) S.E.M was also performed on the specimen. S.E.M results for each specimen are presented below.
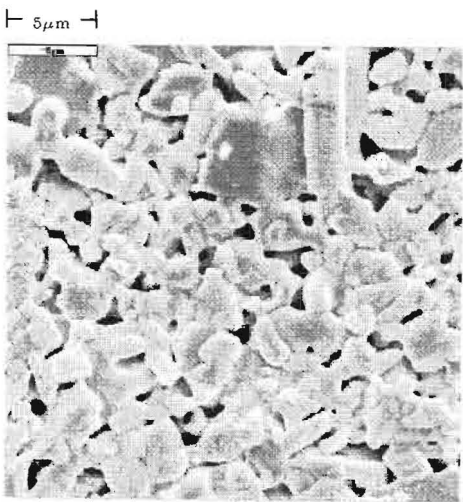
3.3.1 S.E.M and Grain Size Distribution for the YBCO Specimen

Cut Edge - 5000X
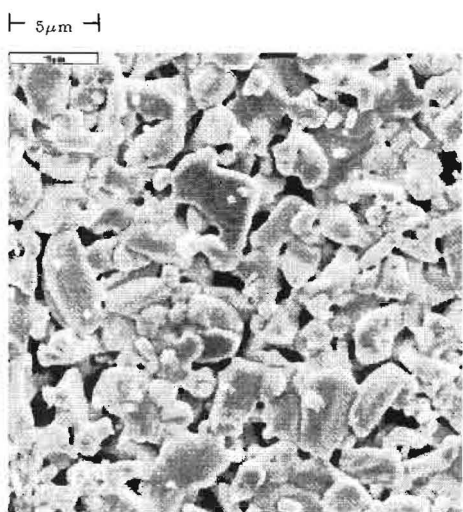
Middle - 5000X

Outer Edge - 5000X

Low Magnification - 1500X

For the YBCO specimen, 135 random grains (from the scans) were selected and the grain diameters a_o measured. A Gaussian fit (red) to the histogram (Fig. 11) yields a mean grain diameter of $a_o = 2 \pm 2\mu$m.
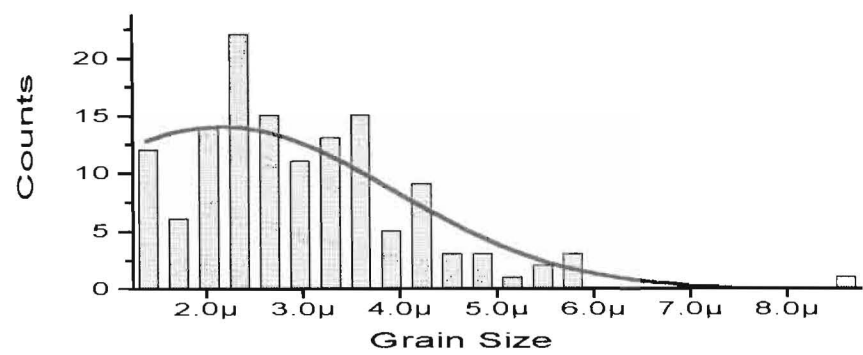
Fig. 11: Grain size distribution for the YBCO specimen
from a sample of 135 random grains.

3.3.2 S.E.M and Grain Size Distribution for the EBCO Specimen
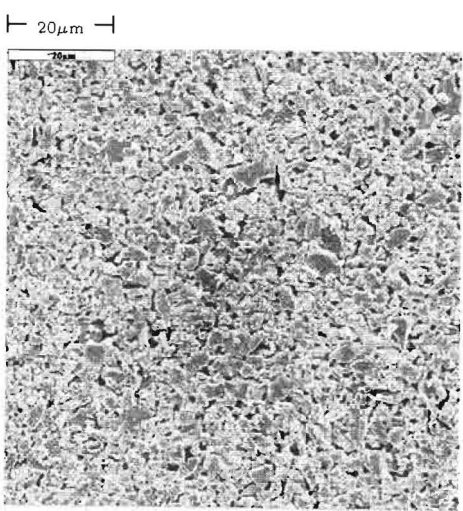

Cut Edge - 5000X

Middle - 5000X

Outer Edge - 5000X   Low Magnification - 1500X
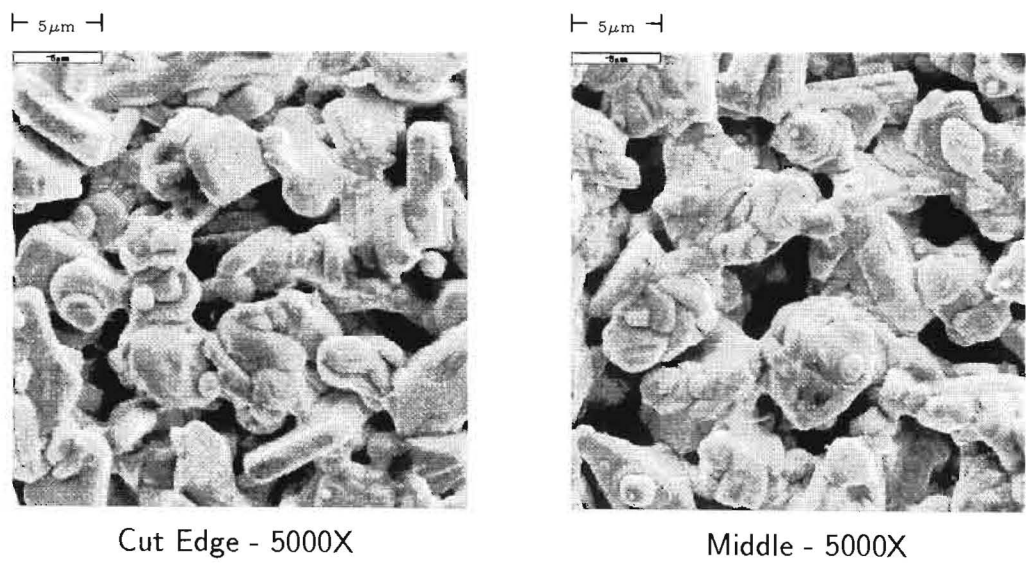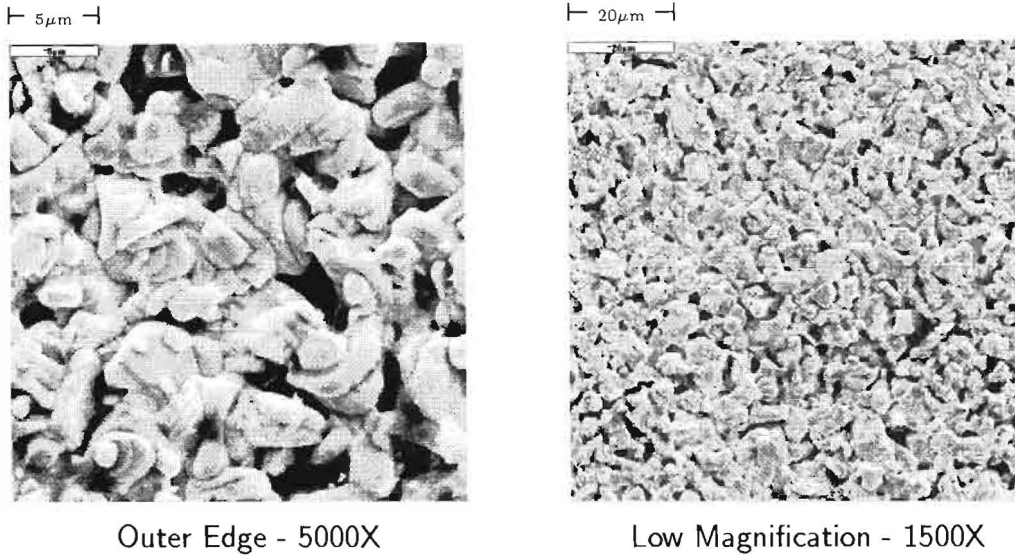
For the EBCO specimen, 104 grains (from the scans) were randomly selected and the grain diameters a_o measured. A Gaussian fit (red) to the histogram (Fig. 12) yields a mean grain diameter of $a_o = 3 \pm 2\mu$m.

Fig. 12: Grain size distribution for the EBCO specimen
from a sample of 104 random grains.

3.3.3 S.E.M and Grain Size Distribution for the C2MIX Specimen
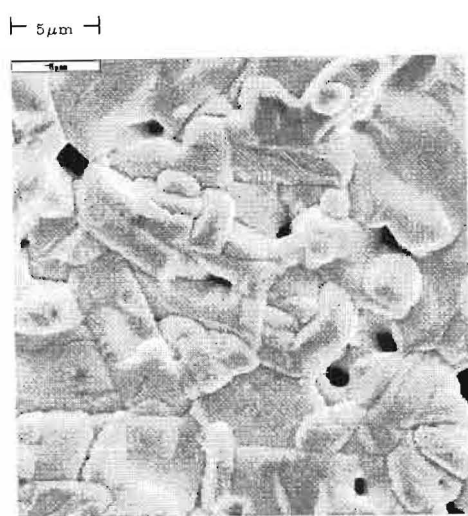
Cut Edge - 5000X
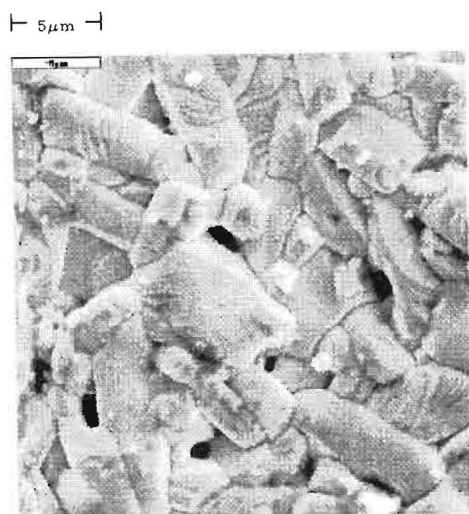
Middle - 5000X

Outer Edge - 5000X
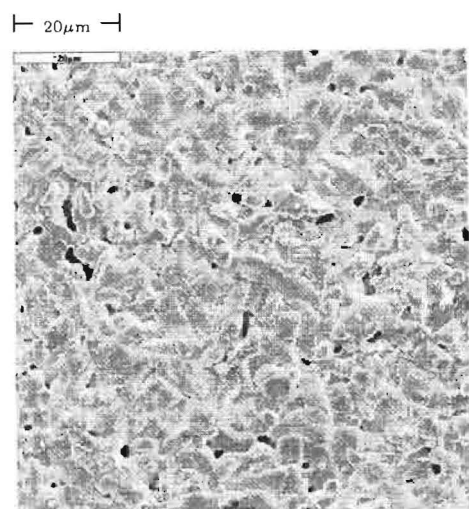
Low Magnification - 1500X

For C2MIX, 74 random grains (from the scans) were selected and the grain diameters a_o measured. A Gaussian fit (red) to the histogram (Fig. 13) yields a mean grain diameter of $a_o = 4 \pm 2 \mu m$.

The SEM's for the C2MIX specimen reflect that this specimen has a much higher density (lower void) than the control specimens. It is, however, unclear as to whether this

39

is due to the difference in sintering temperatures or possibility of better bonding of grains due to the mixed species.
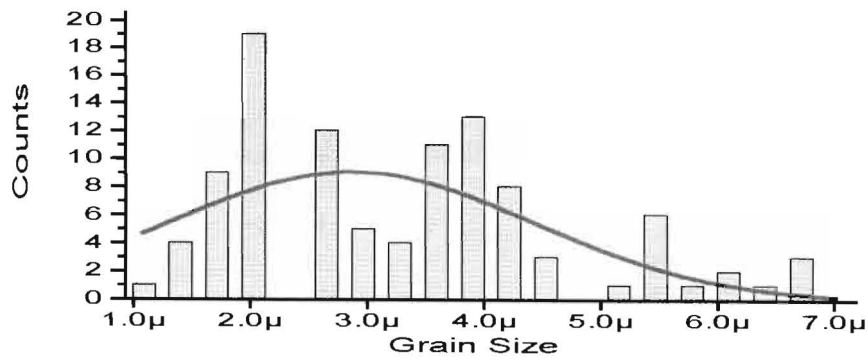

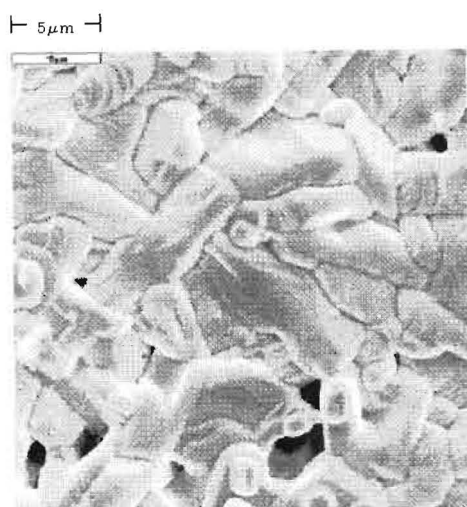Fig. 13: Grain size distribution for the C2MIX specimen from a sample of 74 random grains.

3.4 Description of Experimental Method

3.4.1 Magnetometer
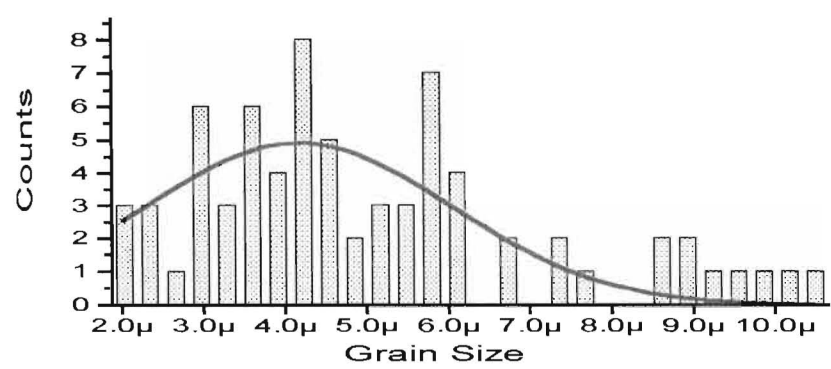
The description of the vibrating-sample magnetometer, used in the present investigation, has been given by Doyle [78]. Here we will focus on the basic operation of the magnetometer. The description that follows is based on the schematic diagram of the electronics used in the vibrating-sample magnetometer, shown in Fig. 14.

An oscillator and power amplifier (A6) drives a mechanical transducer (TR) at a frequency of approximately 82Hz. The two annular capacitor plates (PV) and the specimen (S) which are mechanically coupled by a sample rod (ST), vibrate approximately synchronously with an amplitude of order 0.1-0.3mm. The specimen vibrating in the magnetic field, generated by the solenoid (SM), sets up a time varying component of the field which induces a potential in the detection coils (DC) given by:

$$V_s(t) = \alpha a \nu M \cos(2\pi \nu t + \Phi_s), \tag{57}$$

where α is a geometric constant for the coils (DC), a is the vibration amplitude, ν is the vibration frequency, M is the magnetic moment of the specimen, and Φ_s is the phase of the signal relative to the oscillator (OS).

If $a\nu = constant$, then $V_s = constant \times M \cos(2\pi \nu t + \Phi_s)$. However, it is difficult to keep the vibration amplitude a and the phase ϕ_S constant. This problem is solved by means of the phase-locked loop. Thus the application of a DC potential, V, to the vibrating plates (PV), generates a signal on each of the two stationary plates (PS) of the capacitor which is given by:

$$V_R(t) = \pm \beta a \nu V \cos(2\pi \nu t + \Phi_R), \tag{58}$$

where β is a constant relating to the capacitor geometry, Φ_R is the phase of the signal relative to the oscillator (OSC). Clearly $V_R = constant \times V \cos(2\pi \nu t + \Phi_R)$ if $a\nu = constant$. The reference signal, V_R, is passed through a series of amplifiers A_1, A_2 and an attenuator (AT). Its phase is adjusted with the aid of a switch (SW) and a phase shifter (PS1) in order to be identical with that of the signal V_S for the detection coils.
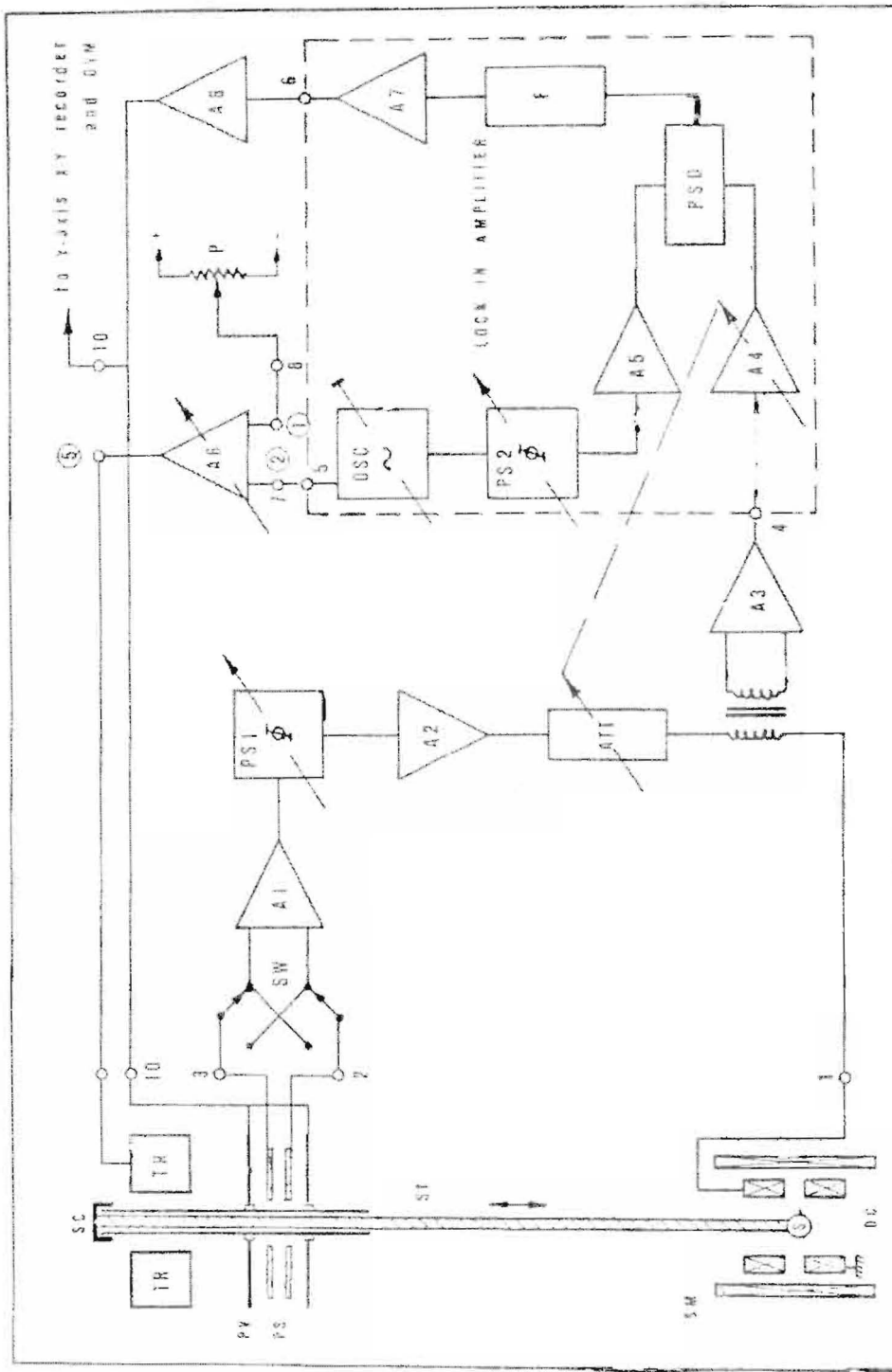
41

Fig. 14: Schematic diagram of the electronics used in the vibrating-sample magnetometer (Due to Doyle [78]).

42

The reference signal V_R is then mixed with V_S in the primary winding of the transformer T. The error signal V_E, across the secondary winding of the transformer T is then given by

$$V_E = V_S - G_1 V_R, \qquad (59)$$

where $G_1 = (GainA_1) \times (GainPS1) \times (GainA_2) \times (GainA_T)$. By adjusting the DC potential V on the vibrating plates PV the error signal V_R may be set to zero.

It follows from Eqs. (57), (58) and (59) that the magnetic moment M is then given by

$$M = AV, \qquad (60)$$

where $A = (G_1 \beta / \alpha)$ is a constant.

This null method therefore gives the magnetic moment directly in terms of the DC potential, V, independently of $a\nu$. In the automatic, phase-locked loop mode, the error signal V_E is amplified in a low noise amplifier A_3 and tuned amplifier A_4, and then synchronously rectified in a phase sensitive detector P.S.D, (driven by the oscillator and amplifier A_5). The DC output of the P.S.D is passed through an adjustable low-pass filter, F, amplified by amplifiers A_7, A_8 and finally applied to the vibrating plates PV. The output voltage from A_8, $-30v < V < +30v$, is advantageous since it allows for the magnetic moment of the specimen to change polarity without having to change the phase of the reference signal, V_R, with the aid of the switch, SW.

$V \propto | V_E |$ or

$$V = \gamma \mid (V_S - G_1 V_R) \mid \times \text{sign}(V_s - G_1 V_R), \qquad (61)$$

where γ is the gain of the detection systems, V_S and V_R are in phase with each other and are given respectively by

$$V_S = \alpha a\nu M cos(2\pi\nu t + \phi_S) \qquad (62)$$

and

$$V_R = \beta a\nu V cos(2\pi\nu t + \phi_R). \qquad (63)$$

From above, it can easily be shown that

$$V = \left[\frac{\gamma\alpha a\nu}{1 + G_1\gamma\beta a\nu} \right] M. \qquad (64)$$

43

If $G_1 \gamma \beta \, a\nu \gg 1$, then

$$M \cong V\left(\frac{\beta G_1}{\alpha}\right) \tag{65}$$

is independent of $a\nu$.

The DC output V which is directly proportional to the magnetic moment M of the specimen, is applied to the Y-axis of the X-Y recorder, and the to computer via the analog-to-digital (A/D) converter for digital signal (data) capture. The magnetisation in emu is obtained by scaling the moment by a multiplicative factor of 4π and dividing by the sample volume.

The power for the Cu solenoid is supplied by a power supply (0-40 A). The solenoid current, and hence the field, H, is obtained by noting the voltage across a precision 0.01Ω, 10W resistor that is connected in series with the solenoid for high currents (for high field magnetisation measurements) and connected across a 0.1Ω, 5W resistor for low currents (for low field magnetisation measurements). This voltage is the sent to the X-axis of the X-Y plotter and to the computer via the A/D card for digital capture of the field (H) data. For a more comprehensive understanding see Ref. [78].

3.4.2 Magnetisation Measurements

Isothermal D.C magnetisation measurements (low and high field) were performed on all specimens, for temperatures ranging from 71.5K to T_c in steps of 1K. The 71.5K ($M-H_a$) curve for each specimen was used to determine the scaling factor for the magnetisation M. The procedure for determining this factor will now be outlined.

For an infinitely long specimen, the initial slope (Meissner region, $B = 0$) of the $M-H_a$ curve is given by $dH/dM \approx -1$. However, for shorter specimens, such as those used in the present investigation, the initial slope is given by $dH/dM \approx -1/(1 - D_m)$, where D_m is the magnetometric demagnetisation coefficient. The value of D_m for all specimens was determined using computer interpolation of tabulated data [79] of demagnetisaion and dimension ratio ($\rho = a/b$), where a and b are the semi-major and semi-minor axes of the rod specimen. Each specimen had a dimension ratio of $\rho = 7.07$, yielding a demagnetisation factor of $D_m = 0.035$. The scaling factor for the magnetisation data was obtained by taking the reciprocal of the initial slope of the $M(H)$ curve.

44

Plots of the scaled data for the family of $M - H_a$ isotherms for each specimen used in the investigation is given in Figs. 15-17. All relevant information, required for use in the critical state model algorithm, were obtained from these ($M - H_a$) isotherms. [Note that the isotherms shown are for H_a increasing only].

3.4.3 Magnetisation results

Plots of magnetisation $(-4\pi M)$ against applied, H_a, for YBCO, EBCO and C2MIX, H_a increasing, are show in Figs. 15-17 below.

Fig. 15: Isothermal d.c. magnetisation $(M - H_a)$ curves

(H_a increasing) for the YBCO specimen,

for 71.5K $\leq T \leq$ 85.5K in 1K steps.

Fig. 16: Isothermal d.c. magnetisation $(M - H_a)$ curves

(H_a increasing) for the EBCO specimen,

for 71.5K $\leq T \leq$ 87.5K in 1K steps.
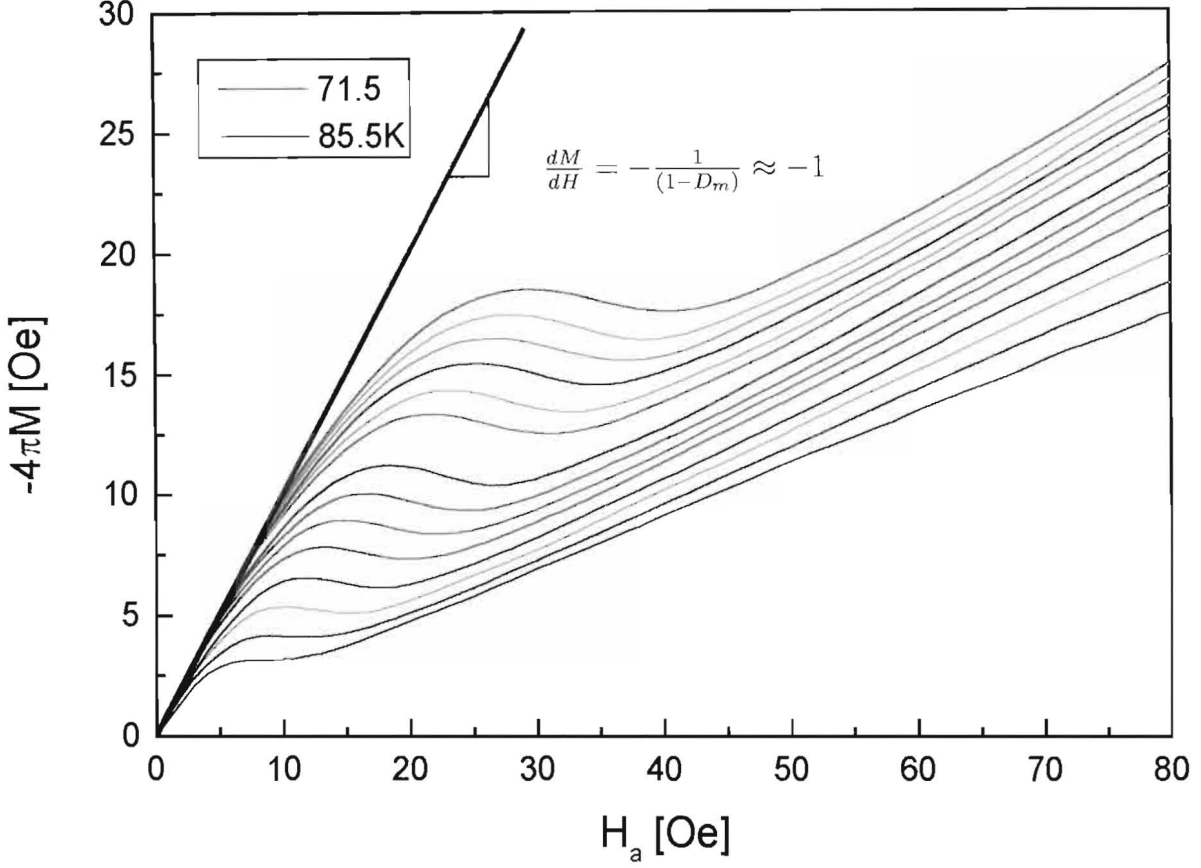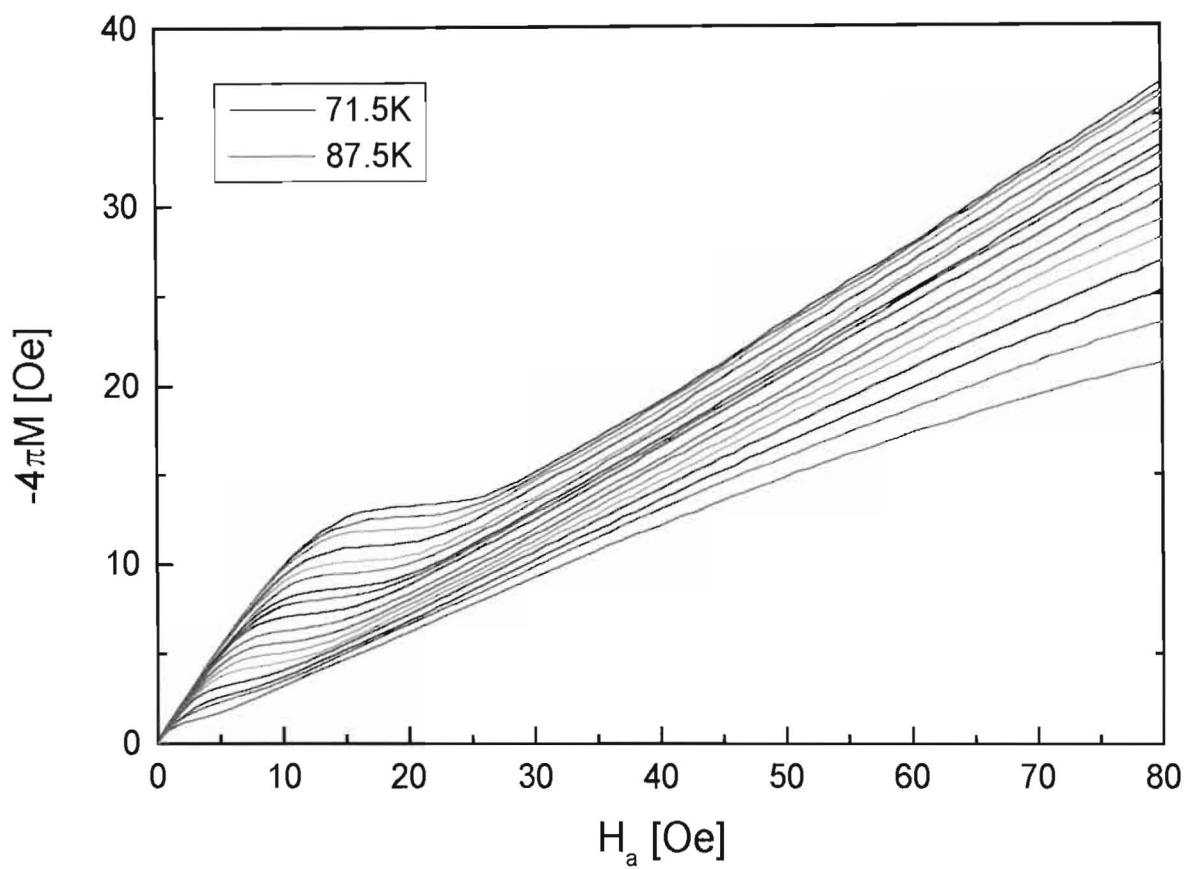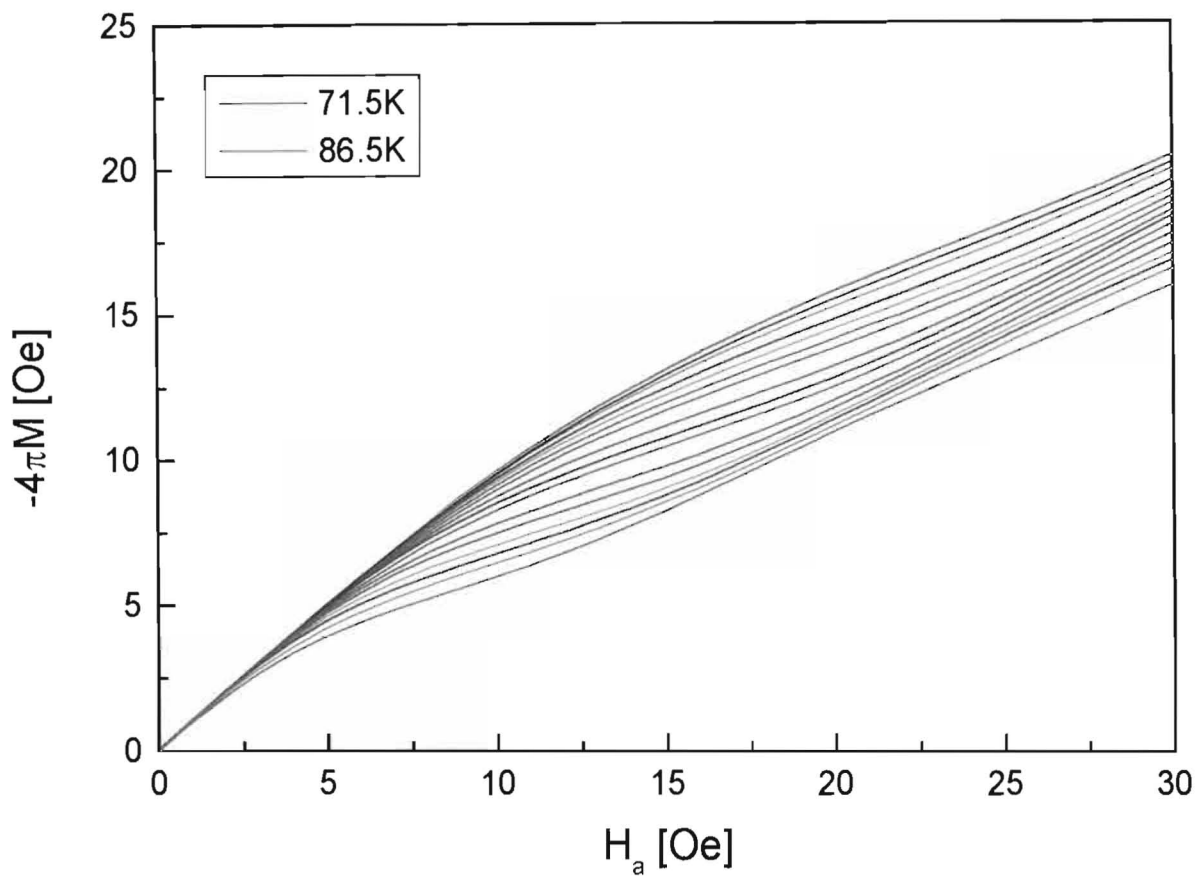
Fig. 17: Isothermal d.c. magnetisation $(M - H_a)$ curves

$(H_a$ increasing) for the C2MIX specimen,

for 71.5K $\leq T \leq$ 86.5K in 1K steps.

4 RESULTS AND DISCUSSION

4.1 Critical State Model Algorithm

The low temperature experimental $M - H_a$ data was fitted to Eqs. (55) and (56) with the aid of a computer algorithm [80] that utilizes a weighted least-squares procedure to ensure a best possible fit to the data. A brief summary of the fitting procedure is given here. For a detailed treatment see Refs. [70, 81] and references therein.

The algorithm first makes an approximate correction for demagnetisation effects by transforming the data to give the internal field:

$$H = H_a \left[1 - D_m (1 - \mu) \right] - 4\pi M D_m, \qquad (66)$$

where D_m is the axial magnetometric demagnetisation factor for a cylindrical right prism, μ is a temperature-dependent permeability for the field range $H_o << H_a < H_{c1g}$, where H_o is junction characteristic field, and M is the specimen magnetisation.

Fig. 18 shows a typical low field $M - H$ plot, data (open circles) and the CSM fit (solid line), for a polycrystalline YBCO specimen due to Doyle $et\ al.$ [70]. Here H_1 and H_2 correspond respectively to the starting and ending of the shoulder region of the $M - H$ curve and are parameters in the fitting algorithm.

The algorithm sets $\mu = 1$ for $H_a < H_1$ and $\mu = \mu_e$ for $H_a > H_2$. For $H_1 < H_a < H_2$, the value of μ is linearly interpolated between 1 and μ_e. The initial value of μ_e, from a fit to the initial un-corrected $M - H$ data at each temperature, is used to iterate to a final value within a specified error. Thus, final values for μ_e, H_o, J_{co}, and δ are obtained for each $M(H)$ isotherm. Note: These four parameters are the minimum number required to perform the fit.
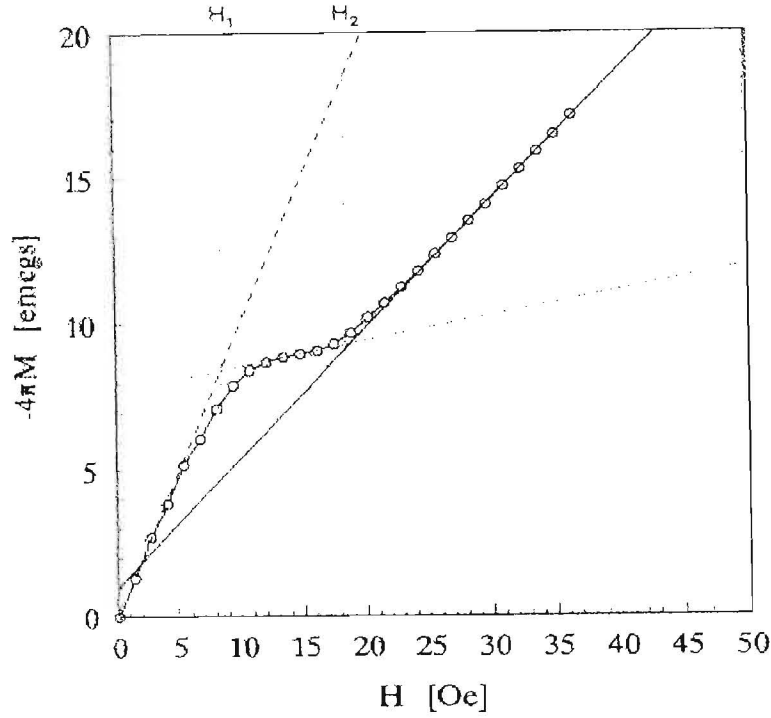
Fig. 18: Critical state model fit (solid line) to typical low-field
magnetisation $(M - H)$ data (open circles)
for a polycrystalline YBCO specimen $(T \approx 68K)$
(from Doyle *et al.* [70]).

4.2 Critical State Model Fits to Experimental Magnetisation

In Figs. 19-21 below, we show the critical state model fits (Eqs. (55) and (56) with $J_{co}(T)$, $\delta(T)$, $H_o(T)$ and $\mu_e(T)$ as free fitting parameters) to the experimental magnetisation (isotherms) for the YBCO, EBCO, and C2MIX specimens for a few temperatures. The open symbols represent the demagnetisation corrected data points, while the solid lines represent the CSM fits to the data. Note: CSM fits to the experimental magnetisation was carried out for temperatures ranging from 71.5K to near T_c, in 1K increments, for each specimen. Listed in Tables 2-4 are the results (values for these free fitting parameters) of the fits given in Figs. 19-21 respectively.
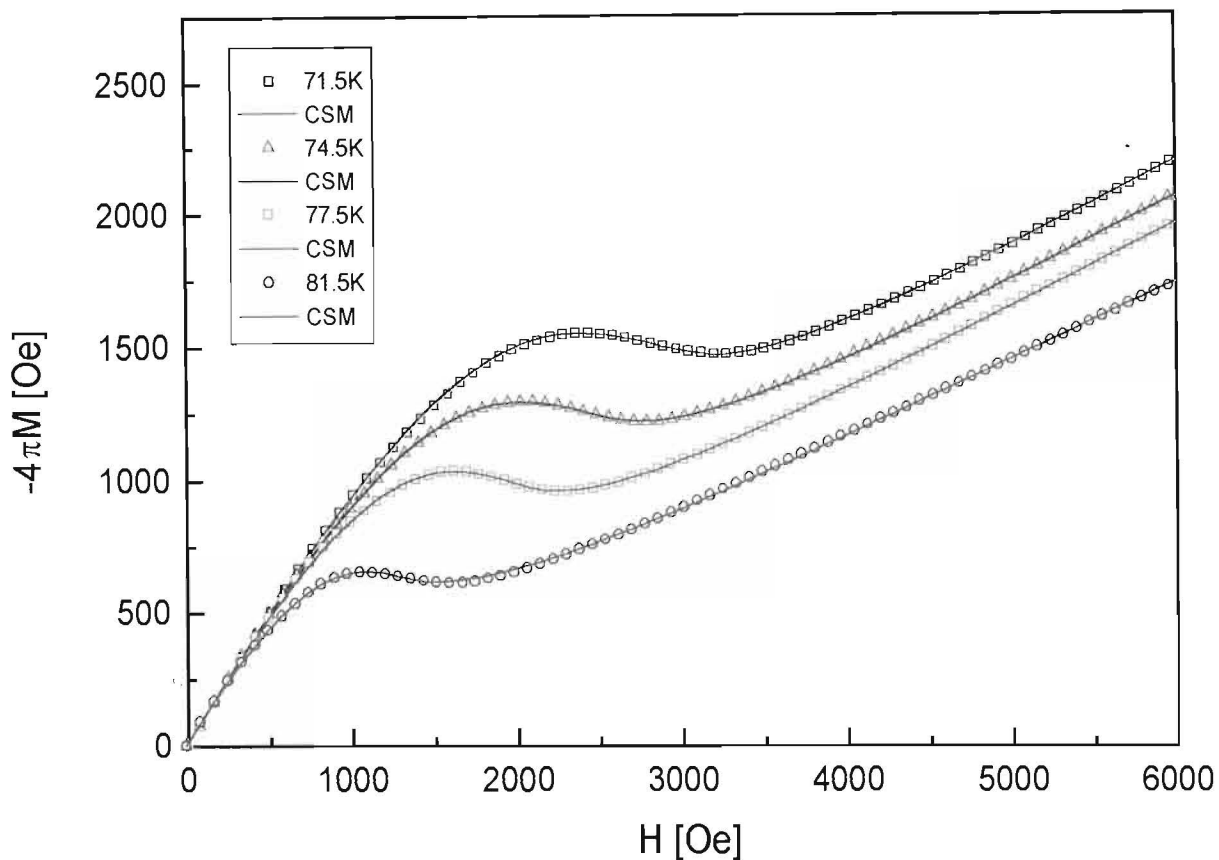
Fig. 19: Critical state model fits (solid lines) to a few representative experimental $(M - H)$ (open symbols) isotherms for the YBCO specimen.

	YBCO			
	71.5K	74.5K	77.5K	81.5K
$J_{co}(T)$ (A.cm^{-2})	2338	1506	1157	579
$\delta(T)$	0.051	0.041	0.031	0.038
$H_o(T)$ (Oe)	11.4	12.1	10.4	8.3
$\mu_e(T)$	0.669	0.675	0.685	0.719

Table 2: Values for the free fitting parameters obtained from the CSM fits to the $M - H$ isotherms in Fig. 19.
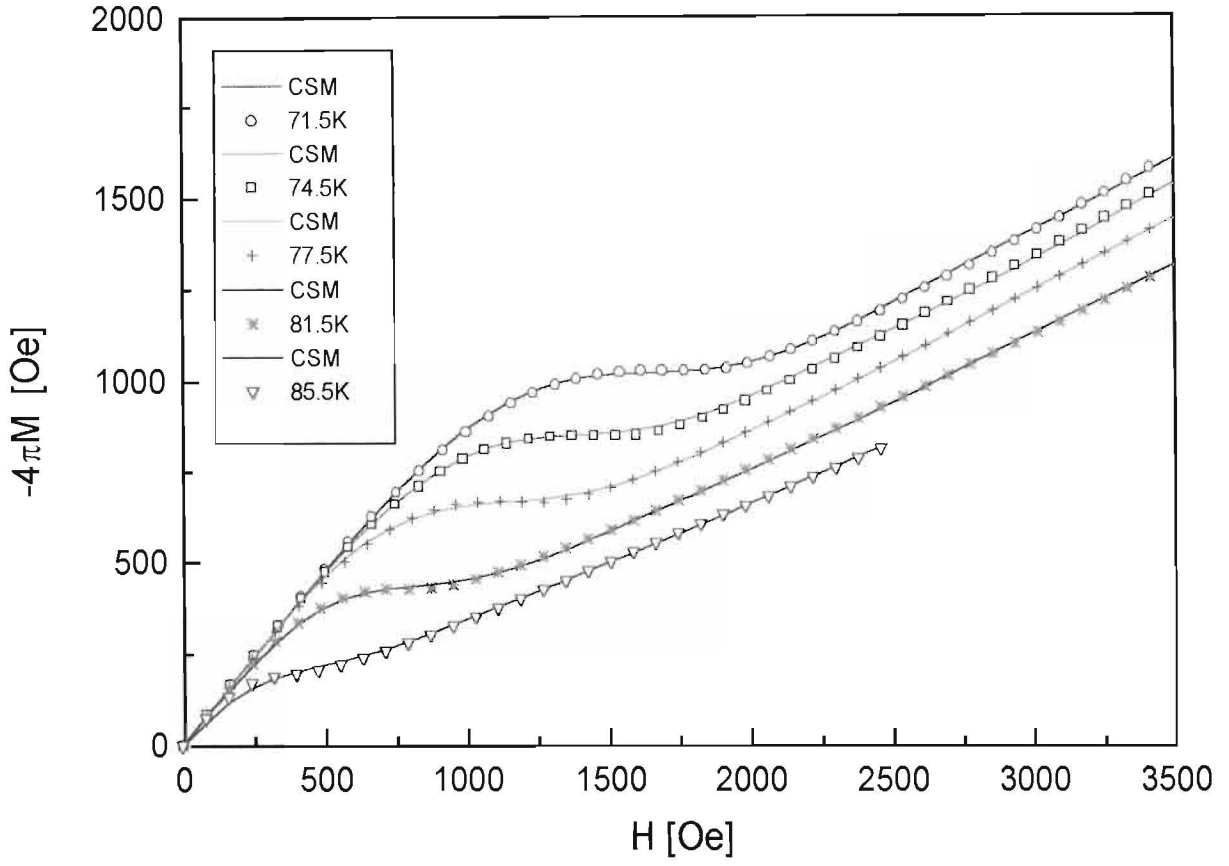
Fig. 20: Critical state model fits (solid lines) to a few representative experimental $(M - H)$ (open symbols) isotherms for the EBCO specimen.

	EBCO				
	71.5K	74.5K	77.5K	81.5K	85.5K
$J_{co}(T)$ (A.cm^{-2})	1991	1368	730	376	91
$\delta(T)$	0.039	0.045	0.047	0.021	0.032
$H_o(T)$ (Oe)	6.0	5.7	5.8	5.0	4.6
$\mu_e(T)$	0.565	0.580	0.597	0.624	0.668

Table 3: Values for the free fitting parameters obtained from the CSM fits to the $M - H$ isotherms in Fig. 20.
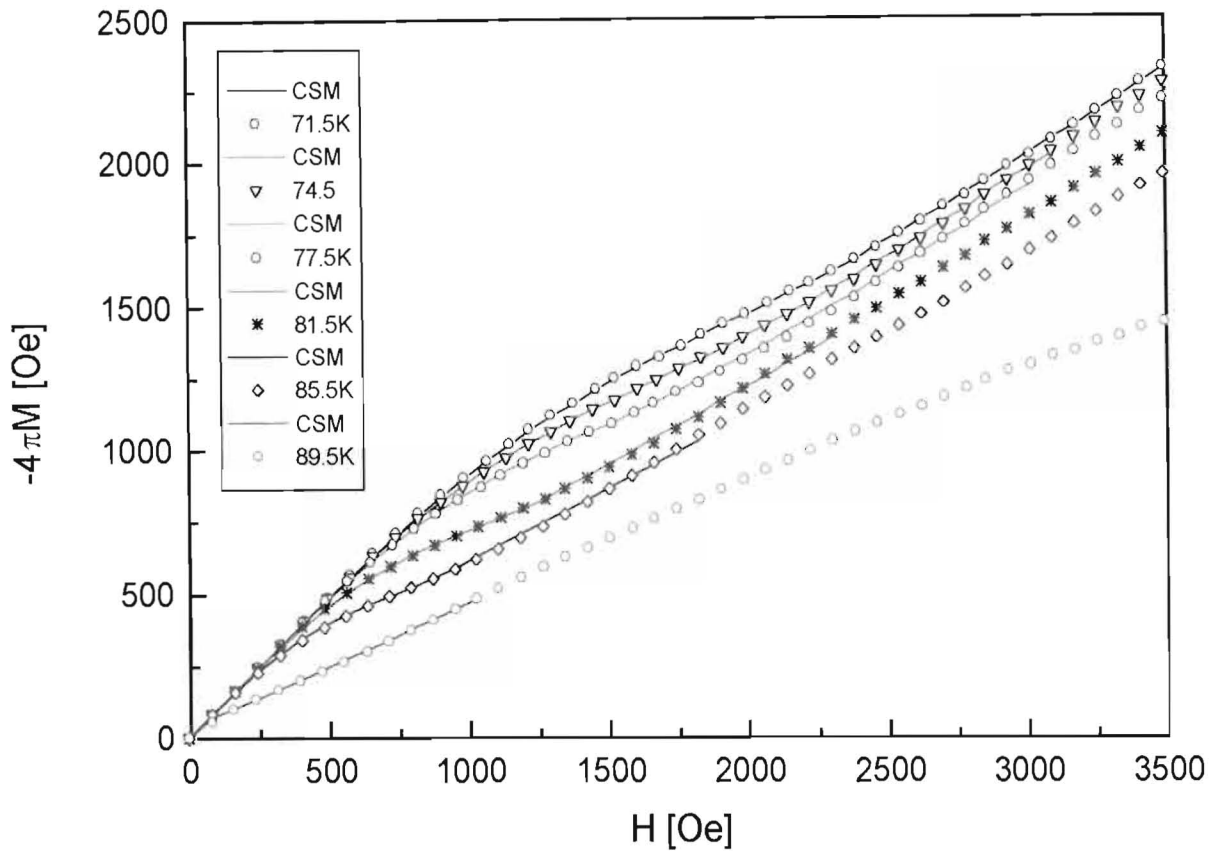
Fig. 21: Critical state model fits (solid lines) to a few representative experimental $(M - H)$ (open symbols) isotherms for the C2MIX specimen.

	C2MIX					
	71.5K	74.5K	77.5K	81.5K	85.5K	89.5K
$J_{co}(T)$ (A.cm^{-2})	2216	1650	1393	785	413	103
$\delta(T)$	0.089	0.100	0.101	0.118	0.191	0.178
$H_o(T)$ (Oe)	4.9	4.6	4.2	3.2	2.1	0.4
$\mu_e(T)$	0.394	0.403	0.416	0.444	0.490	0.558

Table 4: Values for the free fitting parameters obtained from the CSM fits to the $M - H$ isotherms in Fig. 21.

53

4.3 Temperature Dependence of Characteristic Parameters

4.3.1 Effective Permeability - $\mu_e(t)$

For a macroscopically homogeneous specimen with a low grain aspect ratio (i.e. near unity), the specimen can be modeled as a two-dimensional array of closely packed cylindrical grains, of radius $R_g = a_o/2$, parallel to the mean internal field H. In this approximation $\mu_e(t)$ is given by Clem [47], as:

$$\mu_e(t) = f_n + f_s \left[\frac{2I_1(\Lambda)}{\Lambda I_o(\Lambda)} \right], \tag{67}$$

where f_n and f_s are respectively the normal (inter-granular) and superconducting (intra-granular) volume fractions and I_n is the modified Bessel function with $\Lambda = \Lambda(t) \equiv R_g/\lambda_g(t)$, where λ_g is the intra-granular penetration depth. Note: The grain radius R_g for the YBCO, EBCO and C2MIX specimens is respectively 1, 1.5 and 2 μm (see Section 3.3).

Using various forms for the $\lambda_g(t)$ dependence (to be reviewed in detail below), the model given by Eq. (67) is fitted to experimental $\mu_e - t$ data as obtained from the critical state model fits to each $M - H$ isotherm for each specimen. These fits allow for the determination and investigation of a number of additional parameters arising from the various $\lambda_g(t)$ dependences in which they are treated as free fitting parameters. The actual fitting procedure is now discussed in greater detail.

(i) "Trial fit number 1"

The Gorter-Casimir empirical two-fluid model [Eq. (15)] for $\lambda_g(t)$, re-written as

$$\lambda_g(t) = \lambda_g(0)(1 - t^4)^{-1/2}, \tag{68}$$

is used in Eq. (67). Here $\lambda_g(0)$ (the inter-granular penetration depth at $t = 0$), the free volume f_n and the critical temperature T_c are treated as free fitting parameters. Note: $t = T/T_c$.

(ii) "Trial fit number 2"

Here the BCS form for $\lambda_g(T)$ [Eq. (35)], with $T = tT_c$, yeilds

$$\lambda_g(t) = \lambda_g(0)\left[\frac{\Delta(t)}{\Delta(0)}\tanh\left(\frac{\Delta(t)}{2k_B tT_c}\right)\right]^n. \tag{69}$$

Here $n = -1/3$ is appropriate for the "clean-limit" and $n = -1/2$ for "dirty-limit" (see sections 1.10.3 and 1.10.4). Upon substitution of $\Delta(0) = \beta k_B T_c/2$ ([61] and references therein) and re-arrangement of terms, Eq. (69) may be expressed by:

$$\lambda_g(t) = \lambda_g(0)\left[\frac{\Delta(t)}{\Delta(0)}\tanh\left(\frac{\beta}{4t}\frac{\Delta(t)}{\Delta(0)}\right)\right]^n. \tag{70}$$

Eq. (70) is substituted into Eq. (67), which is then fitted to the $\mu_e - t$ data. Here $\Delta(t)/\Delta(0)$, the reduced gap parameter, is obtained by polynomial interpolation of Mühlschlegel's data [82], $\lambda_g(0)$, f_n and T_c take on values obtained from "trial fit number 1", and $\beta = O(1)$ is treated as a free fitting parameter. The "clean-limit" $(n = -1/2)$ as opposed to the "dirty-limit" gives a better fit to the $\mu_e - t$ data.

(iii) "Trial fit number 3"

In this trial fit, Eq. (69), with $\Delta(t) = \alpha k_B T_c(1 - t)^{1/2}$, $\Delta(0) = \beta k_B T_c/2$ ([61] and references therein) and $n = -1/2$ is used in the fitting of Eq. (67) to the $\mu_e - t$ data. Here $\lambda_g(0)$, f_n, T_c and β are values obtained from the previous two trial fits, and α is treated as a free fitting parameter.

The "best" $\mu_e - t$ fit (solid lines in Fig. 22) for each specimen is obtained using "trial fit number 3". Thus, from the above three trial fits, $\lambda_g(0)$, f_n, T_c, β and α are determined, and listed in Table 5.
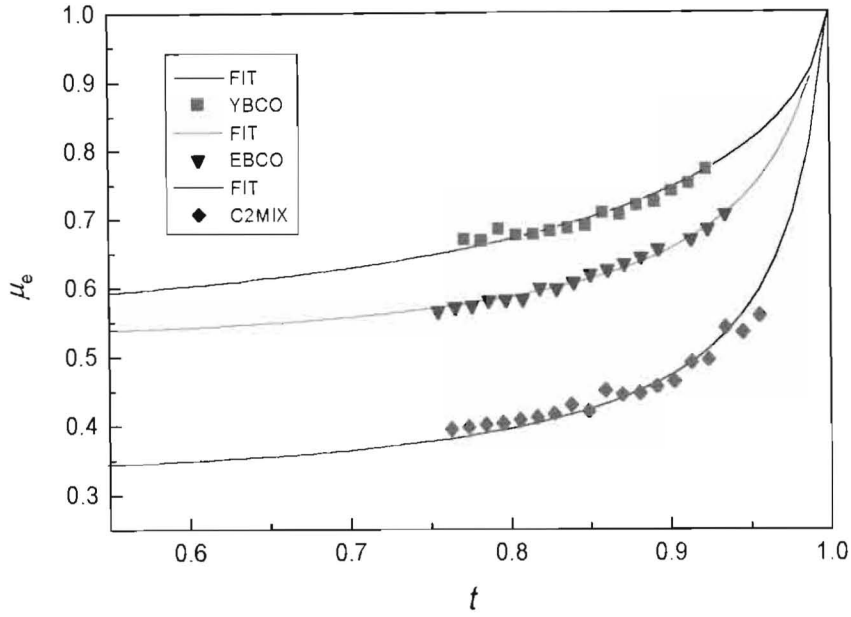
Fig. 22: Model [Eq. (67) - solid lines] for the effective permeability $\mu_e(t)$, fitted to experimental $\mu_e - t$ data (solid symbols) for each specimen. The best fits are obtained using "trial fit number 3".

It is clear from examination of Fig. 22 that the effective permeability for the C2MIX specimen is considerably smaller than that of the two control specimens over the same temperature range. This esentially results from the fact that the C2MIX specimen has a larger average grain radius and a smaller free volume than that of the two control specimens.

	Specimens		
Results	YBCO	EBCO	C2MIX
$\lambda_g(0)(\mu m)$	0.34	0.26	0.29
f_n	0.12	0.31	0.11
T_c (K)	92.5	94.5	93.5
β	5.4	5.4	5.1
α	3.5	4.4	4.1

Table 5: Free fitting parameters, for each specimen, obtained from the various trial fits.

56

4.3.2 Average Josephson-Junction Characteristic Field - $H_o(t)$

The average Josephson-junction (JJ) characteristic field $H_o(t)$ has been modeled in the "short-junction limit" (to be confirmed later), in which the inter-granular penetration depth, λ_j, given by Eq. (38), is larger than the dimension of the grain boundary parallel to the magnetic field B (the grain diameter, a_o, in this case).

For a specimen consisting of a three-dimensional (3D) arrangement of cubic grains (side $a_o = 2R_g$) parallel to the applied field H along the cube side, the Josephson-junction field, H_o, is given by Doyle et al. [83] as:

$$H_o(t) = \eta \frac{B_o}{\mu_e(t)} \cong \eta \frac{\phi_o}{\mu_e(t)\Big[2\lambda_g(t) + d_N\Big]a_o}. \tag{71}$$

Here d_N, the junction barrier thickness (typically a few nm's), and $\eta = O(1)$, a geometrical factor that allows for grain anisotropy, are treated as free fitting parameters. The effective permeability $\mu_e(t)$ is given by Eq. (67), where f_n is taken from "trial fit number 1" and $\lambda_g(t)$ is given by Eq. (69). In Eq. (69), $\lambda_g(0)$ is taken from "trial fit number 1", $\Delta(t) = \alpha k_B T_c (1-t)^{1/2}$, $\Delta(0) = \beta k_B T_c/2$ and $n = -1/2$. Note: T_c, β and α are taken from "trial fits" 1, 2 and 3 respectively (see Section 4.3.1 for details). Fig. 23 shows the model fits [Eq. (71) - solid lines] to experimental $H_o - t$ data for each specimen.
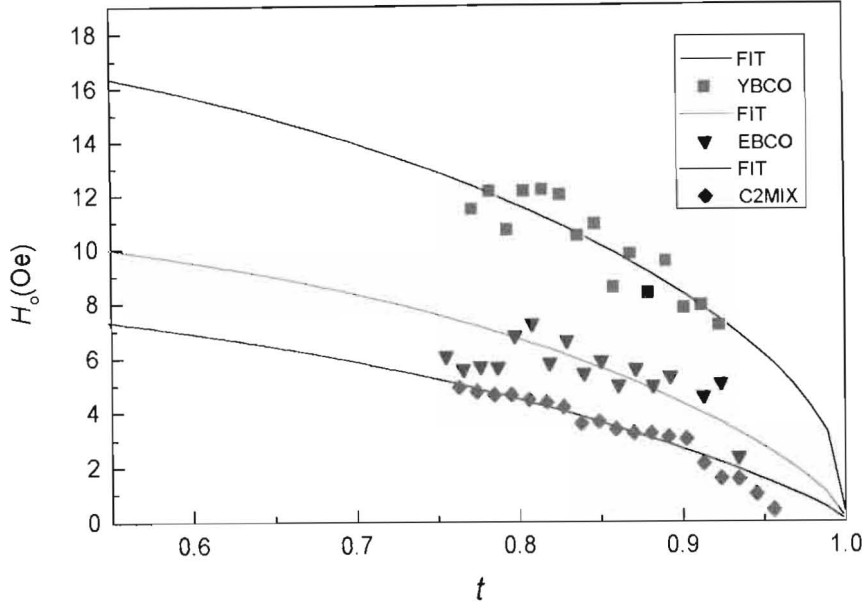
Fig. 23: Model [Eq. (71) - solid lines] for the Josephson-junction characteristic field, fitted to experimental $H_o - t$ data (solid symbols) of each specimen.

The free fitting parameters obtained from the $H_o - t$ fits are listed in Table 6.

	Specimens		
Results	YBCO	EBCO	C2MIX
η	0.74	0.36	0.27
d_N (nm)	1.0	1.0	1.0

Table 6: Free fitting parameters, for each specimen, from the $H_o - t$ fits.

From Fig. 23, it is evident that the mixing of the two control compounds has lowered the Josephson-junction critical field H_o for the entire temperature range under consideration.

The parameter H_o corresponds to the to local magnetic field at which the critical current density, $J_c(H)$, begins fall exponentially (in increasing magnetic field) toward the "plateau region" defined in Section 2.4. Meilikhov [67] also points out that H_o should be inversely proportional to grain size (a_o in the present work), thereby reaffirming the model [Eq.(71)] and supporting the present results. The lowest value for η is obtained for the C2MIX specimen (largest grain size a_o). Although the free fitting parameter d_N is found to be relatively insensitive in fitting process, $d_N \sim 1nm$ seems to give an adequate fit to the $H_o - t$ data of each specimen.

4.3.3 Zero-Field Critical Current Density - $J_{co}(t)$

The Ambegaokar-Baratoff theory [44], for a single S-I-S (Superconductor-Insulator-Superconductor) Josephson tunnel junction, corrected for order parameter suppression at the junction boundaries Deutscher and Müller [84], is given by:

$$J_{co}(t) = \frac{\pi \Delta_i(t)}{2eR_nA} \tanh\left[\frac{\Delta_i(t)}{2k_B t T_c}\right], \tag{72}$$

where $A = a_o^2$ is the effective junction area, R_n is the normal state resistance and Δ_i is the suppressed order parameter at the junction boundary.

The analysis is appropriate for the "inhomogeneous limit" in granular high-T_c ceramic superconductors, in which $\xi(t) \sim a \ll d$, where ξ is the coherence length, a is the atomic spacing and d is the grain size (a_o in the present investigation) [29]. By solving of the non-linear Ginzburg-Landau equation for the order parameter (given the junction boundary condition: $\nabla(\nabla\triangle)_n = -1/b$, where $b \sim \xi_o^2/a \sim a$ is the range over which the order parameter is suppressed and ξ_o is the temperature-independent coherence length, Deutscher [29] shows that the suppressed order parameter, $\Delta_i(t)$, is given by:

$$\Delta_i(t) = \Delta_o(t) \tanh\left[\omega(t)\right], \tag{73}$$

where $\Delta_o(t) = \alpha k_B t T_c$ is the gap parameter far from the junction boundary and $\omega(t) = b/\sqrt{2}\xi_s(t)$, where $\xi_s(t)$ is the effective coherence length in the superconducting material and is give by: $\xi_s(t) = \xi_s(0)(1-t)^{-1/2}$. Written empirically, $\omega(t)$ is given by:

$$\omega(t) = \omega(0)(1-t)^{1/2}, \tag{74}$$

where $\omega(0) = b/\sqrt{2}\xi_s(0)$. Here values for T_c and α were taken from trial fits 1 and 3 respectively (see section 4.3.1 for details), while R_n and $\omega(0)$ were treated as free fitting parameters.
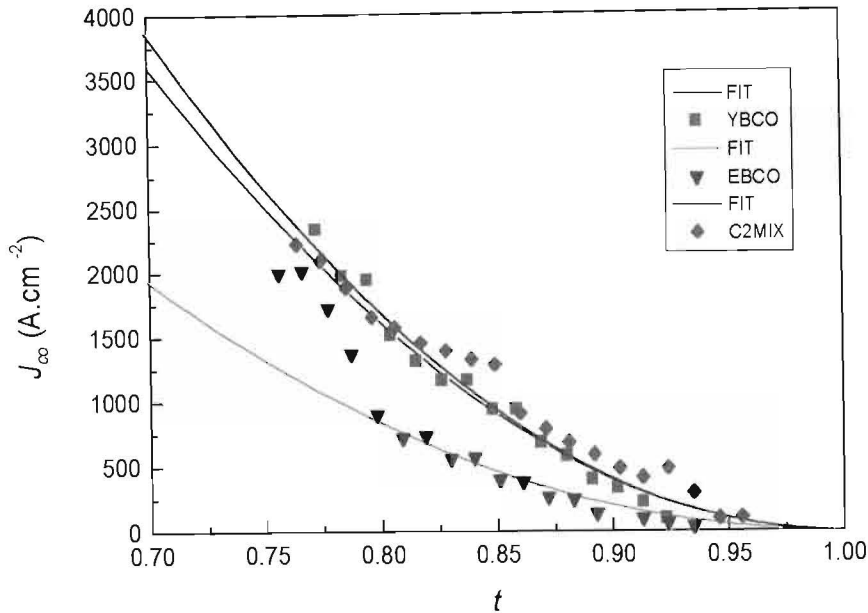
Fig. 24: Ambegaokar-Baratoff model [Eq. (72) - solid lines] for the zero-field critical current density $J_{co}(t)$, fitted to the experimental $J_{co} - t$ data (solid symbols) of each specimen.

We see from Fig. 24 that the Ambegaokar-Baratoff model [Eq. (72) - solid lines] gives a reasonably good fit, over the temperature range $0.75 < t < 0.95$, to the experimental $J_{co} - t$ data, of each specimen, obtained from the CSM fits.

It is apparent that the $J_{co}(t)$ behaviour for the EBCO specimen in the reduced temperature range $(0.75 < t < 0.8)$ exhibits a "step-like" behaviour below $t \cong 0.79$, while for the fit $t > 0.79$ seems to be well behaved. The anomaly has been checked by careful re-fitting, and is not a result of errors in curve fitting. We conclude, therefore, that there is a superconducting phase transition at about 77K ($t \cong 0.79$) in the grain boundaries, due probably to oxygen stoichiometry.

Over the temperature range under consideration, the C2MIX specimen gives slightly higher critical current density than that obtained for the YBCO specimen and a significantly higher critical current density than that obtained for the EBCO specimen. The magnitude of the free fitting parameters obtained from the $J_{co} - t$ fits are listed in Table 7.

	Specimens		
Results	YBCO	EBCO	C2MIX
$R_n(\Omega)$	40	40	10
$\omega(0)$	0.98	0.72	0.80

Table 7: Free fitting parameters, for each specimen, from the $J_{co} - t$ fits.

It is apparent that the mixing of the control compounds has considerably lowered the grain boundary resistance, R_n, while $\omega(0)$ has taken on an intermediate value. Our values for $\omega(0)$ range from 0.72 to 0.98, which compare well with values obtained elsewhere ([81] and references therein).

Other relevant values such as $\Delta_o(0)$, $2\Delta_o(0)/kT_c$, $\Delta_i(0)$ and $\Delta_i(77K)$ were obtained by polynomial interpolation and are listed in Table 8.

	Specimens		
	YBCO	EBCO	C2MIX
$J_{co}(77K)$ (A.cm^{-2})	1 130	715	1 180
$J_{co}(0)$ (A.cm^{-2})	17 300	10 300	19 600
$\Delta_o(0)$ (meV)	28	35	33
$2\Delta_o(0)/kT_c$	7.0	8.7	8.2
$\Delta_i(0)$ (meV)	20.9	21.9	21.9
$\Delta_i(77K)$ (mev)	4.3	4.6	4.3

Table 8: Other important values obtained by polynomial interpolation.

Values for $\Delta_o(0)$ and $2\Delta_o(0)/kT_c$ of 28 meV and 7.0 respectively for the YBCO specimen compare well with 29 meV and 7.3 respectively obtained elsewhere [81]. The C2MIX specimen has a value for $\Delta_o(0)$ (gap parameter far from the junction boundary at $t = 0$) that is intermediate between that obtained for the YBCO and EBCO specimens. The reduced gap parameter, $2\Delta_o(0)/kT_c$, for the C2MIX specimen has a value of 8.2, which is close to the value of 8.7 obtained for the EBCO specimen. Incidentally, all the reduced

gap parameters fall within the prediction for the strong-coupling limit for these super-conductors (see [81] and references therein). The intrinsic gap parameter at the junction boundary $\Delta_i(77K)$ =4.3 meV, for the C2MIX specimen, is equal to that obtained for the YBCO specimen.

We now look at the Josephson penetration depth, λ_j, and in particular to show that our model H_o for the "short-junction limit" ($\lambda_j \geq a_o$), in the present study, is fully justified. Model expressions for μ_e [Eq. (67)] and J_{co} [Eq. (72)] are used in Eq. (38) which is then interpolated to obtain values for λ_j for each specimen at 0 and 77K. These are given in Table 9.

	Specimens		
Results	YBCO	EBCO	C2MIX
$\lambda_j(77K)(\mu\text{m})$	43	75	37
$\lambda_j(0)(\mu\text{m})$	12	22	11

Table 9: Interpolated values of λ_j, for each specimen, at 0 and 77K.

It is apparent that $\lambda_j(0)$ value for each specimen is larger than its respective grain diameter a_o. Note: The grain diameters a_o for the YBCO, EBCO and C2MIX specimens are 2, 3 and 4 μm respectively). Based on the fact that λ_j diverges at T_c [47], it clear that the "short-junction limit" is more than adequately satisfied for each specimen over the entire temperature range up to T_c.

4.3.4 Reduced Field-Independent Component of the Critical Current Density - $\delta(t)$

The parameter δ (related to structural fluctuations in the grain boundaries [52, 67, 68]) is strongly dependent on the specimen morphology [61] and is, therefore, is a useful parameter in the study of the properties of grain boundary weak-link behaviour in high-T_c ceramics.

The temperature dependence of δ, however, is not explicitly given in its definition [Eq. (50)]. It depends implicitly on the temperature dependence of charge carrier density in the grain boundary junctions (GBJ's), and, in particular, on the charge state of the Cu atoms in the Cu-O chains and CuO_2 planes (See section 1.11.2). Fig. 25 shows δ (for each specimen), as obtained from the CSM fits, against the reduced temperature t. The near-T_c behaviour is expected because all length scales are diverging near T_c (see Sections 1.8.2 and 1.8.3).

It is evident from Fig. 25 that for most of the temperature range for which we have results namely, $(0.75 < t < 0.9)$, δ is approximately constant with a value of approximately 0.05 for the two control specimens and approximately 0.10 for the C2MIX specimen. According to Eq. (50) $\delta \propto 1/a_o$. Now, in the present work, the grain diameter, a_o, for the C2MIX specimen is roughly double that of the two control specimens. We are therefore confident that the approximate two-fold increase in δ is genuinely due to improvement in the inter-granular weak-link properties of the C2MIX specimen, and is not a consequence of the grain size differences between the specimens. The present considerations suggest that if the C2MIX specimen had roughly the same grain size as that of the two control specimens, the value of δ for the C2MIX specimen would have been four times larger than for the control specimens.
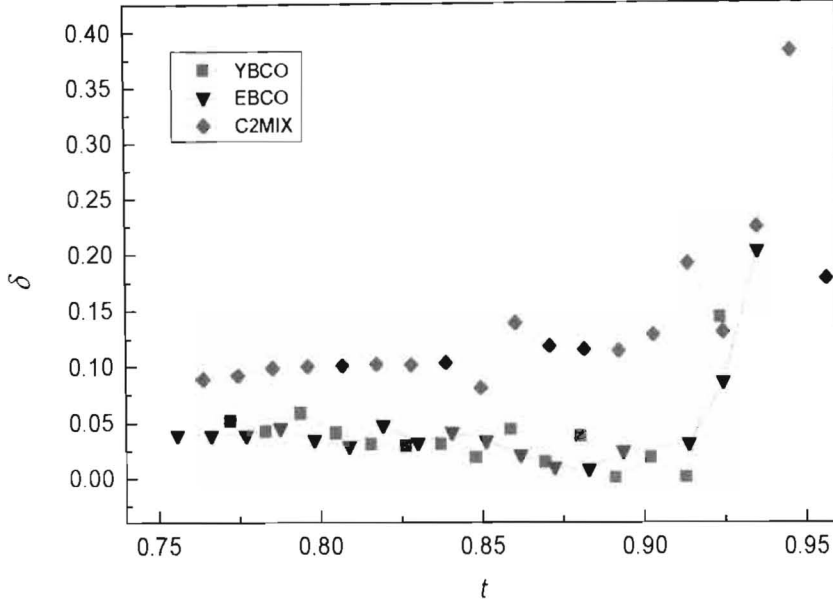
63

Fig. 25: Temperature dependence of δ for the three specimens as indicated on the figure.

The δ ($= J_1/J_0$) parameter represents the height of the plateau region (i.e. the magnetic field region over which the critical current density is independent of the magnetic field - see Section 2.4) and can have a maximum value of 1.0. Meilikhov's analysis [68] shows that the plateau height can, ideally, be increased by increasing the values of both the correlation radius r_o and the r.m.s fluctuation of the critical current ψ (arising from random spatial inhomogeneities in the grain boundary junctions). He suggests that this be achieved through the development of some "technological procedure" [67].

The fact that we have successfully increased the plateau height by approximately two-fold in the C2MIX specimen compared with the two control specimens, suggests that we have probably increased the correlation radius and/or the r.m.s fluctuations of the critical current. This has been achieved by the "mixing" and suitable annealing of two precursor superconducting control compounds (YBCO and EBCO), and is possibly related to an interchange of the Yttrium (Y) and Europium (Eu) atoms in the grain boundaries. This is expected to allow for an improvement in the quality of the grain boundaries.

Fig. 26 is a plot of $J_{co}\delta(= J_1)$ (the field-independent component of the critical current density or plateau critical current density) against the reduced temperature, t.

64

For all t, in the measurement range, $J_{co}\delta$ for the C2MIX specimen is higher than the values obtained for either of the two control specimens. It is also clear from Fig. 26 that the plateau critical current density for the C2MIX specimen decreases linearly with reduced temperature t, and approximately quadratically with t for the two control specimens (within experimental scatter).
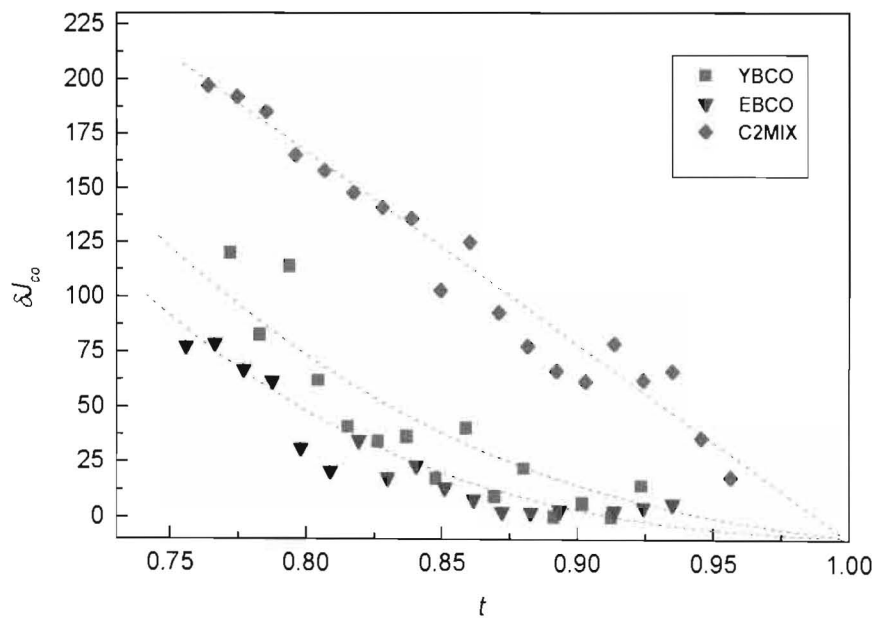

Fig. 26: Temperature dependence of $J_{co}\delta$ for each of the specimens. The dashed lines are a guide to the eye.

5 CONCLUSION

The effect of mixing has yielded slightly higher $J_{co}(t)$ values in addition to considerably lowering the normal state resistance, R_n, of the grain boundary junction. Reduced gap parameters ($2\Delta_o(0)/k_B T_c$) for each specimen fall within the strong-coupling region for these materials. The value of 8.2 obtained for the C2MIX specimen is close to the maximum value of 8.7 obtained for EBCO, implying that the effect of mixing has not significantly reduced the strength of the superconducting Cooper-pairs.

Meilikhov [68] has commented that apart from raising the overall critical current density of high-T_c superconductors, is of practical importance to be able to maintain high critical current densities in the presence of relatively high magnetic fields. The effect of mixing has increased the overall critical current density, but the increase is primarily due an increase in the field-independent component of the critical current density $J_{co}\delta$ (see Fig. 26). The ratio $J_1/J_0 = \delta$ (the plateau height), increased from roughly 0.05 for the two control specimens to approximately 0.1 for the C2MIX specimen.

We know from $\delta \approx (2r_o/a_o)^{1/2}\psi$ [Eq. (50)] that the plateau height is inversely proportional to $a_o^{1/2}$. Thus, we would have preferred the grain size for the C2MIX specimen to be smaller than that of the two control specimens (YBCO and EBCO), but, in fact, it turned out to be larger. Despite this, we still obtain an approximately two-fold increase in the plateau height δ. We are, therefore, confident that this increase in δ is due to an increase in the correlation radius r_o and/or the r.m.s. fluctuation of the critical current in the grain boundary junctions ψ. We propose that if we are able to produce a mixed specimen with the same grain size as that of the two control specimens, a four-fold increase in δ may be achieved.

The present work is a novel technique (to the best of our knowledge) that demonstrates that the mixing of polycrystalline superconducting ceramic oxides is a promising exercise for increasing the field-independent critical current densities in bulk-sintered specimens. It is possible that stresses have been relieved in the grain boundaries of the C2MIX specimen through some degree of re-arrangement of the Yttrium (Y) and Europium (Eu) atoms (along the grain boundaries), thus reducing the grain boundary energy. This may, in fact, have minimized, to a certain extent, the fraction of "bad or poor" inter-granular

weak-links [68].

More work needs to be done to fully explore the potential of this technique of "mixing". This could entail the investigation of how grain boundary parameters and plateau critical current densities respond to: (1) different ratios of Y:Eu; (2) different sintering and annealing programs (different grain sizes); (3) the introduction of dopant atoms (halogens at various concentrations) into mixed specimen; (4) mixing of other superconducting compounds.

The attainment of high field-independent critical current densities, possibly through techniques such as the one used in the present investigation, would be an important step towards the commercial application of superconductors like YBCO.

References

[1] H.K. Onnes, *Commun. Phys. Lab. Univ. Leiden* No. 124c (1911)

[2] M. Cyrot and D. Pavuna, In: *Introduction to Superconductivity and High-T_c Materials*, 4, World Scientific Publishing, (1992)

[3] M. Cyrot and D. Pavuna, In: *Introduction to Superconductivity and High-T_c Materials*, 10, World Scientific Publishing, (1992)

[4] J.G. Bednorz and K.H. Müller, *Z. Phys.* B **64** (1986) 189

[5] M.K. Wu, J.R. Ashburn and C.J. Torng and P.H. Hor, R.L. Meng, L. Gao, Z.J. Huang, Y.Q. Wang, and C.W. Chu, *Phys. Rev. Lett.* **58** (1987) 908

[6] C.W. Chu, L. Gao, F. Chen, Z.J. Huang, R.L. Meng and Y.Y. Xue, *Nature* **365** (1993) 323

[7] C. Kittel, In: *Introduction to Solid State Physics*, 6th ed, 321, John Wiley and Sons Ltd, (1986)

[8] C. Kittel, In: *Introduction to Solid State Physics*, 6th ed, 322-323, John Wiley and Sons Ltd, (1986)

[9] M. Tinkham, In: *Introduction to Superconductivity*, J. Shira and E. Castellano, 2nd ed, 3, McGraw-Hill Publishing Company, (1996)

[10] F. London and H. London, *Proc. R. Soc.* A **149** (1935) 71

[11] C.J. Gorter and H.B.G. Casimir, *Z. Phys.* **35** (1934) 963

[12] M. Cyrot and D. Pavuna, In: *Introduction to Superconductivity and High-T_c Materials*, 50-53, World Scientific Publishing, (1992)

[13] D.R. Tilley and J. Tilley, In: *Superfluidity and Superconductivity*, D.F. Brewer, 3rd ed, 19, Institute of Physics Publishing, Reprinted (1996)(pbk)

[14] D.R. Tilley and J. Tilley, In: *Superfluidity and Superconductivity*, D.F. Brewer, 3rd ed, 20, Institute of Physics Publishing, Reprinted (1996)(pbk)

[15] V.L. Ginzburg and L.D. Landau, *Zh. Eksp. Teor. Fiz.* (in Russian) **20** (1950) 1064

[16] M. Tinkham, In: *Introduction to Superconductivity*, J. Shira and E. Castellano, 2nd ed, 110-117, McGraw-Hill Publishing Company, (1996)

[17] M. Cyrot and D. Pavuna, In: *Introduction to Superconductivity and High-T_c Materials*, 58-60, World Scientific Publishing, (1992)

[18] M. Cyrot and D. Pavuna, In: *Introduction to Superconductivity and High-T_c Materials*, 60-62, World Scientific Publishing, (1992)

[19] M. Tinkham, In: *Introduction to Superconductivity*, J. Shira and E. Castellano, 2nd ed, 110-113, McGraw-Hill Publishing Company, (1996)

[20] I.M. Firth, In: *Superconductivity*, J.G. Cook, 20-21, Mills and Boon Limited, (1972)

[21] C. Kittel, In: *Introduction to Solid State Physics*, 6th ed, 324, John Wiley and Sons Ltd, (1986)

[22] A.A. Abrikosov, *Zh. Eksp. Teor. Fiz.* **32** (1957) 1442; [*Sov. Phys. - JETP* **5** (1957) 1174]

[23] B. Raveau, *Physics Today*, October (1992) 53

[24] D.R. Tilley and J. Tilley, In: *Superfluidity and Superconductivity*, D.F. Brewer, 3rd ed, 25, Institute of Physics Publishing, Reprinted (1996)(pbk)

[25] M. Cyrot and D. Pavuna, In: *Introduction to Superconductivity and High-T_c Materials*, 104-123, World Scientific Publishing, (1992)

[26] M. Tinkham, In: *Introduction to Superconductivity*, J. Shira and E. Castellano, 2nd ed, 64, McGraw-Hill Publishing Company, 1996

[27] M. Tinkham, In: *Introduction to Superconductivity*, J. Shira and E. Castellano, 2nd ed, 103, McGraw-Hill, Publishing Company, 1996

[28] M. Cyrot and D. Pavuna, In: *Introduction to Superconductivity and High-T_c Materials*, 8-10, World Scientific Publishing, (1992)

[29] G. Deutscher, In: *Early and Recent Aspects of Superconductivity*, J.G. Bednorz and K.A. Müller, **90**, 174-199, Springer-Verlag, Berlin, (1989) (and references therein)

[30] M. Cyrot and D. Pavuna, In: *Introduction to Superconductivity and High-T_c Materials*, 168, World Scientific Publishing, (1992)

[31] M. Cyrot and D. Pavuna, In: *Introduction to Superconductivity and High-T_c Materials*, 169-182, World Scientific Publishing, (1992)

[32] J.R. Waldram, In: *Superconductivity of Metals and Cuprates*, 222-223, Institute of Physics Publishing, (1996)

[33] C. Kittel, In: *Introduction to Solid State Physics*, 6th ed, 639, John Wiley and Sons Ltd, (1986)

[34] G. Burns, In: *High-Temperature Superconductivity: An Introduction*, 78, Academic Press Inc, (1992)

[35] J.M. Tarascon, L.H Greene, B.G. Bagley, W.R. McKinnon, P. Barboux and G.W. Hull, In: *Novel Superconductivity*, S.A. Wolf and V.Z. Kresin, 713, Plenum Press, New York, (1987)

[36] J.R. Waldram, In: *Superconductivity of Metals and Cuprates*, 270, Institute of Physics Publishing, (1996)

[37] W.D. Callister Jr, In: *Materials Science and Engineering: An Introduction*, W. Anderson, 5th ed, 51-52, John Wiley and Sons Inc, 605 Third Avenue New York, (2000)

[38] W.D. Callister Jr, In: *Materials Science and Engineering: An Introduction*, W. Anderson, 5th ed, 78, John Wiley and Sons Inc, 605 Third Avenue New York, (2000)

[39] S.M. Allen and E.L. Thomas, In: *The Structure of Materials*, W. Anderson, 327-330, John Wiley and Sons Inc, 605 Third Avenue New York, (1999)

[40] W.D. Callister Jr, In: *Materials Science and Engineering: An Introduction*, W. Anderson, 5th ed, 80, John Wiley and Sons Inc, 605 Third Avenue New York, (2000)

[41] R.L. Peterson and J.W. Ekin, *Phys. Rev. B* **37** (1988) 9848

[42] M. Cyrot and D. Pavuna, In: *Introduction to Superconductivity and High-T_c Materials*, 42-44, World Scientific Publishing, (1992)

[43] M. Cyrot and D. Pavuna, In: *Introduction to Superconductivity and High-T_c Materials*, 130-145, World Scientific Publishing, (1992)

[44] V. Ambegaokar and A. Baratoff, *Phys. Rev. Lett.* **10** (1963) 486; erratum, *Phys. Rev. Lett.* **11** (1963) 104

[45] M. Cyrot and D. Pavuna, In: *Introduction to Superconductivity and High-T_c Materials*, 143, World Scientific Publishing, (1992)

[46] J.F. Kwak, E.L. Venturini, D.S. Ginley, and W. Fu, In: *Novel Superconductivity*, S.A. Wolf and V.Z. Kresin, 983-991 Plenum Press, New York, (1987)

[47] J.R. Clem, *Physica C* **153-155** (1988) 50

[48] T.R. Dinger, T.K. Worthington, W.J. Gallagher, and R.L. Sandstrom, *Phys. Rev. Lett.* **58** (1987) 2687

[49] P. Chaudhari, R.H. Koch, R.B. Laibowitz, T.R. McGuire, and R.J. Gambino, *Phys. Rev. Lett.* **58** (1987) 2684

[50] J.W. Ekin *et al.*, *J. Appl. Phys.* **62** (1987) 4821

[51] M. Murakami, *Supercond. Sci. Technol.* **5** (1992) 185

[52] I.K. Yanson, *Sov. Phys. - JEPT* **31** (1970) 808; [*Zh. Eksp. Teor. Fiz.* **58** (1970) 1511]

[53] P. Chaudhari, J. Mannhart, D. Dimos, C.C. Tsuei, J. Chi, M.M. Oprysko, and M. Scheuermann, *Phys. Rev. Lett.* **60** (1988) 1653

[54] G. Paterno, C. Alvani, S. Casadio, U. Gambardella, and L. Maritato, *Appl. Phys. Lett.* **53** (1988) 609

[55] J.F. Kwak, E.L. Venturini, P.J. Nigrey and D.S. Ginley, *Phys. Rev. B* **37** (1988) 9749

[56] D. Dimos, P. Chaudhari, J. Mannhart, F.K. LeGoues, *Phys. Rev. Lett.* **61** (1988) 219

[57] D. Dimos, P. Chaudhari, J. Mannhart, *Phys. Rev. B* **41** (1990) 4038

[58] J. Mannhart, P. Chaudhari, D. Dimos, C.C. Tsuei, and T.R. McGuire, *Phys. Rev. Lett.* **61** (1988) 2476

[59] K.K. Likharev, *Rev. Mod. Phys.* **51** (1979) 101

[60] Xiao-jun Yu and M. Sayer, *Phys. Rev. B* **44** (1991) 2348

[61] T.B. Doyle and R.A. Doyle, *Phys. Rev. B* **47** (1993) 8111

[62] S.E. Babcock and D.C. Larbalestier, *App. Phys. Lett.* **55** (1989) 393

[63] J. Jung, M.A.-K. Mohamed, S.C. Cheng, and J.P. Franck, *Phys. Rev. B* **42** (1990) 6181

[64] A.L.L. Jarvis and T.B. Doyle, In: *Proc. EUCAS' 97 Applied Superconductivity Conference*, The Netherlands, June 1997, *Inst. Phys. Conf. Ser.* **158** (1997) pp 1149-1152

[65] E.Z. Meilikhov and T.B. Doyle, In: *Proc. 7th Intl. Critical Currents Workshop*, Alpbac, January 1994 *J. Supercond.*

[66] S. Jin, T.H. Tiefel, R.A. Fastnacht, and G.W. Kammlott, *Appl. Phys. Lett.* **60** (1992) 3307

[67] E.Z. Meilikhov, *Supercond.* **3** (1990) 1110

[68] E.Z. Meilikhov, *Physics - Uspekhi* **36** (1993) 129

[69] W.D. Callister Jr, In: *Materials Science and Engineering: An Introduction*, W. Anderson, 5th ed, 84, John Wiley and Sons Inc, 605 Third Avenue New York, (2000)

[70] T.B. Doyle, R.A. Doyle, D. Minkov, V.N. Stepankin, and U.P. Yakovets, *Physica C* **233** (1994) 253

[71] J.W. Ekin, H.R. Hart, Jr, and A.R. Gaddipati, *J. Appl. Phys.* **68** 2285

[72] W.D. Callister Jr, In: *Materials Science and Engineering: An Introduction*, W. Anderson, 5th ed, 436, John Wiley and Sons Inc, 605 Third Avenue New York, (2000)

[73] J.M.D. Coey and K. Donnelly, *Z. Phys. B* **67** (1987) 513

[74] A. Freimuth *et al.*, *Z. Phys. B* **68** (1987) 433

[75] C. Jiang, Yu Mei, S.M. Green, H.L. Luo, and C.Politis, *Z. Phys. B* **68** (1987) 15

[76] M.G. Kanatzidis and T.J. Marks, H.O. Marcy, W.J. McCarthy, and C.R. Kannewurf, *Solid State Commun.* **65** (1988) 1333

[77] H. Dersch and G. Blatter, *Phys. Rev. B* **38** (1988) 11 391

[78] T.B. Doyle, *Ph.D. Thesis*, University of the Witwatersrand, 28-40, 1975 (unpublished)

[79] W.F. Brown, In: *Magnetostatic Principles in Ferromagnetism*, North-Holland Publishing Company, Amsterdam, (1962)

[80] D. Minkov and T.B. Doyle, In: *Proc. 7th Intl. Critical Currents Workshop*, Alpbac, January 1994 *J. Supercond.*

[81] T.B. Doyle and R.A. Doyle, *Cryogenics* **32** (1992) 1019

[82] B. Mühlschlegel, *Z. Physik* **155** (1959) 313

[83] T.B. Dolye, R.A. Doyle, D. Minkov, V.N. Stepankin, and U.P. Yakovets, (unpublished)

[84] G. Deutscher and K.A. Müller, *Phys. Rev. Lett.* **59** (1987) 1745